



Sulfide interlayered cobalt-based oxynitrides for efficient oxygen evolution reaction in neutral pH water and seawater

Ahmed Badreldin^a, Jehad Abed^{b,c}, Noor Hassan^a, Abdellatif El-Ghenymy^a, Wafa Suwaileh^a, Yiming Wubulikasimu^a, Zafar Khan Ghouri^e, Karim Youssef^d, Dharmesh Kumar^d, Khaled Elsaid^a, Edward H. Sargent^b, Ahmed Abdel-Wahab^{a,*}

^a Chemical Engineering Program, Texas A&M University at Qatar, P.O. Box 23874, Doha, Qatar

^b Department of Electrical and Computer Engineering, University of Toronto, Toronto, Ontario M5S 3G4, Canada

^c Department of Materials Science and Engineering, University of Toronto, Toronto, Ontario M5S 3E4, Canada

^d Qatar Shell Research and Technology Centre, P.O. Box 3747, Doha, Qatar

^e International Center for Chemical and Biological Sciences, HEJ Research Institute of Chemistry, University of Karachi, Karachi 75270, Pakistan

ARTICLE INFO

Keywords:

Impure water electrolysis
Electrochemical water oxidation
Oxygen evolution reaction
Neutral pH water electrolysis
Seawater electrolysis

ABSTRACT

Sluggish kinetics of the anodic oxygen evolution reaction (OER) and minor upstream upsets in feed water quality remain bottlenecks for efficient water electrolysis, which is exacerbated under near-neutral pH environments due to H₂O dissociation. In this work, we report the introduction of a NiS_x interlayer in a Co-(NiFe) oxide/nitride catalyst on nickel foam substrate. Postmortem OER characterization in neutral pH synthetic seawater (SSW) shows that stable cationic [Co-(NiFe)]^{δ+} and anionic [O-N]^{δ-} surface species coupled with the NiS_x interlayer accelerate H₂O dissociation, thereby enhancing activity and kinetics. The electrocatalysts exhibit stable performance at 100 mA cm⁻² for 50 h in alkaline and neutral pH SSW with 350 and 425 mV of overpotential, respectively. The faradaic efficiency of the NiS_x interlayer catalysts is enhanced by 10.3% and 8.5% achieving 94.5% and 87.4% under alkaline and neutral pH SSW, respectively, during chronoamperometry tests at a high applied voltage of 1.75 V (vs. RHE).

1. Introduction

Hydrogen is seen as an integral element in our sustainable economy of the future [1]. Of particular interest is green H₂ produced from electrochemical water splitting, where the reaction is driven by renewable electricity produced from the sun or wind [2]. Because of the growing stress on freshwater resources around the globe, seawater has been lately considered as a replacement feedstock for water splitting. However, today's state-of-the-art water electrolyzers mandate stand-alone water desalination and deionization system to purify water feed for durable electrolysis. It has been argued that the large implementation of such indirect seawater electrolysis (ISWE) may result in negative environmental impact associated with brine discharge and carbon footprint [3]. Therefore, a myriad of research on direct seawater electrolysis (DSWE) emerged in recent years proposing solutions to produce H₂ from vastly available seawater reserves without a water purification step.

There are a number of problems slowing the deployment of DSWE such as the shortened lifetime of electrocatalysts due to impurity poisoning, formation of Mg²⁺ and Ca²⁺ precipitates damaging the membrane and electrodes, and undesired anodic chlorine evolution reaction (CER) – a kinetically-favored 2e⁻ anodic side reaction. However, the aforementioned holistic point pertaining to the abundance of seawater as feed for decentralized water electrolysis has continued to propel research into the area. The debate over DSWE versus ISWE has been building up in relevant research [4,5]. However, due to the lack of commercial DSWE electrolyzers to compare with their ISWE electrolyzer counterparts, the wrangle is expected to exist for some time.

Interestingly, a principal reason behind stack failure in conventional water electrolyzers remains to be pertaining to water quality issues that may arise from any upstream upsets during seawater desalination and deionization or cationic impurities from corroding pipes or stack components [6]. Therefore, designing earth-abundant electrocatalysts that are compatible and effective with seawater as a harsh water source

* Corresponding author.

E-mail address: ahmed.wahab@qatar.tamu.edu (A. Abdel-Wahab).

<https://doi.org/10.1016/j.apcatb.2023.122599>

Received 7 November 2022; Received in revised form 6 January 2023; Accepted 6 March 2023

Available online 11 March 2023

0926-3373/© 2023 The Authors. Published by Elsevier B.V. This is an open access article under the CC BY license (<http://creativecommons.org/licenses/by/4.0/>).

allows their implementation as ultra-stable and reliable alternatives to costly noble-metal based electrocatalysts in conventional electrolyzers. The choice of reaction environment plays a key role in diminishing the deleterious impacts of these impurities. For instance, using neutral pH water provides a global reaction environment that is less corrosive and more cost-effective than alkaline and acidic electrolytes, hence more appealing for large-scale industrial operation [7]. Moreover, under neutral or near-neutral pH operation using groundwater, river water, or seawater feedstocks, the precipitation of Mg^{2+} and Ca^{2+} impurities can be suppressed, advertently enhancing the performance durability of both electrocatalysts and membranes [8]. However, there are a few challenges pertaining to the design of efficient and durable electrocatalysts for neutral pH electrolytes. First, neutral pH incurs large overpotentials at high current densities due to a kinetically-demanding H_2O dissociation step during the oxygen evolution reaction (OER) [8]. Second, the presence of Cl^- anions in neutral seawater limits the thermodynamic potential window favoring OER over CER compared to alkaline electrolytes [9], which narrows even further as the reaction proceeds due to a drop in the local pH near the anode [10]. There has been an array of anode material development towards improving OER activity on oxides [11], perovskites [12], nitrides [13], sulfides [14], carbon-based [15,16], and phosphides [17], however activity is not the only concern when operating using Cl^- containing electrolytes. Finally, the presence of chloride disables the electrocatalyst due to the irreversible adsorption of Cl^- on active sites and consequent oxidation [18]. Therefore, it is evident that novel design strategies of electrocatalysts are needed for the realization of near-neutral and neutral pH water and seawater impurity-agnostic splitting at scale.

Several design strategies have been demonstrated to suppress chloride oxidation on OER electrocatalysts such as the utilization of carbon sheaths, amorphous oxide overlayers [19], or innately resilient nitrides and sulfide surfaces [20,21]. For example, Kuang et al. incorporated buried sulfide interlayers in benchmark NiFe layered double hydroxide (NiFe LDH) to extend the stability under harsh alkaline saline (6 M KOH + 1.5 M NaCl) water oxidation [22]. Building on their work, Li et al. have investigated the role of metaborate interlayers within γ -(Ni,Fe) OOH multi-layered oxygen evolution electrodes (MOEE) on the stability under alkaline saline (1 M KOH + 0.5 M NaCl) water oxidation [23]. In both works, polyanionic sulfate or metaborate species were found to act as an electrostatic repellent to incoming Cl^- effectively suppressing CER and chloride corrosion. Of particular interest to this work, development of anodic materials for saline neutral pH operation typically suffers from considerable loss in activity and stability. For example, benchmark alkaline OER NiFe LDH showed substantial loss in activity under near-neutral pH borate buffered saline electrolyte (0.3 M borate buffer + 0.5 M NaCl; pH 9.2) whereby chronoamperometric (CA) operation at 10 mA cm^{-2} for 60 min resulted in a sharp increase in applied potential requirement from 1.7 to 2.4 V (vs. RHE) [24]. In our recent work on investigating effective neutral pH cathodes for HER in saline electrolytes, we developed a nickel-vanadium oxynitride atop nickel foam (NVN@NF) which exhibited benchmark Pt-like activities and high stability in neutral pH saline (1 M PB + 0.6 M NaCl) electrolytes [25]. The main aspect of our study focused on ensuring surface heterointerfaces capable of activating more docile H^{6+} -OH $^{6-}$ dissociation and simultaneously suppressing chloride-induced deactivation. This was anticipated to work due to the charge delocalization effect from highly anionic $[\text{N-O}]^{6-}$ coupled with highly cationic $[\text{NiV}]^{6+}$. Surface terminating anionic groups further contributed to electrostatic shielding from corrosive Cl^- , thus ensuring high stabilities under high current densities of -50 and -100 mA cm^{-2} in neutral pH saline electrolyte. Coupling this with first-principle density functional theory (DFT) calculations done by Niu et al., it was found that H_2O dissociation preferentially occurs on the oxide character of $\text{Ni}_3\text{N}/\text{MoO}_2$, followed by reaction propagation on the nitride character of the electrocatalyst [26].

In this work, we report the synthesis of a novel Co-NiFe oxynitride (Co-(NiFe)N) with a buried NiS_x interlayer to synchronously ensure OER

selectivity and enhance stability, whilst maintaining high activity in neutral pH synthetic seawater (35 g/L SSW). It has been rationalized that due to the significant local pH drop near the anode during operation, utilization of Ni as the predominant active site may lower stability due to high dissolution from local acidity. Thus, we use a predominant Co-based surface to reduce metal dissolution due to the significant drop in local pH near the anode during operation. The synergistic nature of oxynitrides can improve corrosion resistance like nitrides while having strong H_2O dissociation thermodynamics similar to oxides. In our recent studies on S,B-codoped binary [27] and ternary oxyhydroxides [28], we found that binary oxyhydroxides show favorable activities in alkaline conditions for OER, while ternary oxyhydroxides exhibit more desired activities and stabilities in near-neutral pH conditions. Herein, we screen the electrocatalytic performance of Co-(NiFe)-based electrocatalysts in neutral pH SSW, containing all major cationic and anionic seawater impurities, and alkaline saline (0.6 M NaCl) electrolyte. The best candidate Co-(NiFe)N@ NiS_x @NF demonstrated overpotentials of 350 and 430 mV in alkaline and neutral pH synthetic seawater electrolytes at a current density of 100 mA cm^{-2} . According to the Pourbaix diagram, under neutral pH (pH 7), the thermodynamic limiting potential for CER to hypochlorous acid (HClO) is 1.701 V (vs. SHE). As a result, the evaluation of reaction selectivity should be conducted at an applied potential well above 1.701 V (vs. SHE). We conducted CA stability and selectivity tests at an applied potential of 1.75 V (vs. RHE) under neutral pH synthetic seawater conditions. Co-(NiFe)N@ NiS_x @NF exhibited 55.5% higher current retention relative to its Co-(NiFe)N@NF counterpart without an NiS_x interlayer. The effect of NiS_x on OER selectivity was also investigated via online gas chromatography (GC) analysis, whereby the interlayered sample attained 94.5% and 88.6% OER FE under alkaline and neutral pH synthetic seawater, respectively, at 100 mA cm^{-2} , relative to 86.2% and 75.8% OER FE for the non-interlayered sample. Textural, surface chemistry, and electrochemical characterizations including HRTEM, FESEM, XAS, XPS, XRD, BET, ECSA, and EIS were employed to explain the increased activity and stability of Co-(NiFe)N@ NiS_x @NF under neutral pH synthetic seawater conditions. Pre- and postmortem OER characterization through XPS and XRD was also conducted to effectively shed light on the nature of NiS_x interlayers during electrolysis.

2. Experimental

2.1. Chemicals and materials

Cobalt (II) acetate tetrahydrate ($\text{Co}(\text{CH}_3\text{CO}_2)_2 \cdot 4 \text{H}_2\text{O}$, analytical reagent), nickel (II) nitrate hexahydrate ($\text{Ni}(\text{NO}_3)_2 \cdot 6 \text{H}_2\text{O}$, analytical reagent), nickel (II) chloride hexahydrate ($\text{NiCl}_2 \cdot 6 \text{H}_2\text{O}$, analytical reagents), iron (III) nitrate nonahydrate ($\text{Fe}(\text{NO}_3)_3 \cdot 9 \text{H}_2\text{O}$, analytical reagent), ammonium hydroxide (NH_4OH), anhydrous toluene ($\text{C}_6\text{H}_5\text{CH}_3$, 99.8%), urea ($\text{CO}(\text{NH}_2)_2$), sulfur (S_8 , 99.998% trace metal basis), potassium hydroxide (KOH), dimethyl sulfoxide (DMSO, $(\text{CH}_3)_2\text{SO}$), sulfuric acid (H_2SO_4), monopotassium phosphate (KH_2PO_4), dipotassium phosphate (K_2HPO_4), and sodium chloride (NaCl) were all purchased from Sigma-Aldrich. KOH was dissolved in deionized water (DIW) to acquire the desired molar concentrations of alkaline electrolytes. 35 g/L of aquarium salt (Aquaforest® Reef Salt) was dissolved in DIW and used as synthetic seawater to mimic real seawater. Appropriate concentrations of KH_2PO_4 and K_2HPO_4 were dissolved in DIW to attain 1 M phosphate buffer (PB) at a pH = 7. DIW for all experiments was acquired through the Millipore (18.2 M Ω cm) purified water system.

2.2. Preparation of electrocatalysts

To grow the NiS_x interlayer on NF, a hydrothermal method was used whereby pretreated NF was first prepared. In a typical procedure, a piece of NF was initially pretreated through tip sonication for 5 min in a 1.5 M H_2SO_4 solution in DIW. The pretreated NF was thoroughly rinsed in DIW

several times before further use. 8 mmol of S_8 powder was thoroughly dissolved in 70 mL of anhydrous toluene, followed by light stirring with two pieces (1.8×5) cm^2 of pretreated NF. After 30 min of stirring, this was transferred to a 100 mL Teflon-lined stainless-steel autoclave and consequently solvothermal treatment was initiated for 6 h at $150^\circ C$ in a programmable oven. The resultant dark-gray $NiS_x@NF$ solids were thoroughly washed with DIW and left to air dry overnight before further use. Separately, 0.15 M $Co(CH_3COO)_2 \cdot 4 H_2O$, 0.23 M $Ni(NO_3)_2 \cdot 6 H_2O$, and 0.08 M $Fe(NO_3)_3 \cdot 9 H_2O$ were dissolved in 64 mL of DIW under stirring. The two pieces of $NiS_x@NF$ from the previous step were added upon dissolution metallic salts and light stirring was allowed for 5 min, followed by addition of 0.056 mol urea. 200 μL of NH_4OH were added dropwise under light stirring, followed by 16 mL of DMSO which acts as an oxide layer inhibitor during hydrothermal treatment. Briefly, under mildly alkaline conditions DMSO ($(CH_3)_2S$) is expected to self-dissociate (i.e., $2(CH_3)_2S \rightleftharpoons (CH_3)_2SOH^+ + CH_3SOCH_2^-$) and elevate the basicity of the solution resulting in excess anionic hydroxides [29]. This phenomenon can be rationalized to act as metal oxide scavengers by suppressing generation of the metal oxide during the synthesis process. The 80 mL solution was transferred again to a 100 mL Teflon-lined stainless-steel autoclave and underwent hydrothermal treatment at $115^\circ C$ for 6 h. To this point, the attained $Co-(NiFe)O_x@NiS_x@NF$ was rinsed with DIW and left to air-dry overnight. Chemical transformation of the top oxide layer to an oxynitride followed a urea-assisted nitridation method, whereby each $1.8 \times 5 cm^2$ $Co-(NiFe)O_x@NiS_x@NF$ sample was placed vertically standing in a downstream alumina crucible in a programmable tubular furnace. 4 g of urea in a different crucible was placed in the furnace upstream the sample, following Argon flow at a flowrate of $50 cm^3 min^{-1}$. This nitridation process was undertaken at $470^\circ C$ for 2 h, with a heating rate of $15^\circ C min^{-1}$. The resultant $Co-(NiFe)N@NiS_x@NF$ was rinsed with DIW and left to air-dry overnight before any electrochemical testing was performed. Scheme 1 illustrates this synthesis method. For contrasting the effect of NiS_x interlayer, the same synthesis process was undertaken without the hydrothermal sulfurization step.

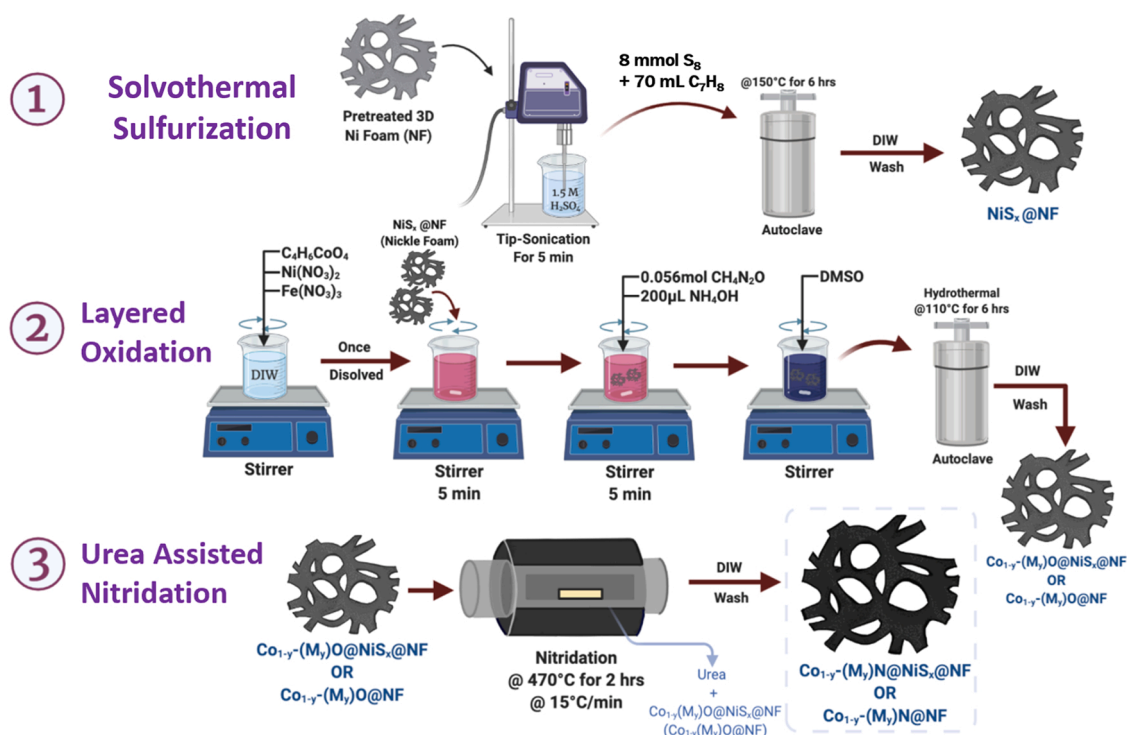
Powder samples for XAS, HRTEM, and BET analyses were prepared using the aforementioned procedure involving sulfurization, layered

oxide growth, and nitridation but with using a starting amount of Ni nanoparticles (NPs) in the absence of NF. The Ni NPs were prepared using a molar amount of $NiCl_2 \cdot 6 H_2O$ equivalent to NF typically used. The Ni NPs were prepared through a physicochemical reduction method using $NaBH_4$ [30]. The Ni NPs then underwent the same pretreatment protocol used on NF to remove any residual surface oxides. This yielded $Co-(NiFe)N@NiS_x@Ni$ and $Co-(NiFe)N@Ni$ as powder counterparts to $Co-(NiFe)N@NiS_x@NF$ and $Co-(NiFe)N@NF$, respectively. $Co-(NiFe)O@NF/Ni$ and $Co-(NiFe)O@NiS_x@NF/Ni$ control samples for Raman and XAS analyses were synthesized under the same aforementioned procedure, with the absence of the nitridation step. Instead, to ensure the same temperature-induced crystallinity effect of nitridation, without the presence of nitride character, calcination was undertaken in air following the same heating program used for nitridation. Similarly, control samples of $Co-(Ni)N@NiS_x@NF$, $Co-(Fe)N@NiS_x@NF$, and $(NiFe)N@NiS_x@NF$ were prepared under the same aforementioned methodology. Briefly, $NiS_x@NF$ samples were prepared and used as growth substrates during the hydrothermal layered oxide growth step, where one metal salt was left out for each control sample and concentrations of the two remaining metal salts were maintained.

Commercial IrO_2/C (Fuel Cell Store, 20 wt%) were drop-casted on pretreated NF by a previously reported method. Briefly, the ink was prepared by 1-hour ultrasonication of 20 mg of IrO_2/C , 540 μL of ethanol, 400 μL of DIW, and 60 μL of 5% Nafion-117. The dispersion was then drop-casted on a predefined area of NF and air dried overnight to attain a catalyst loading of $\sim 2 mg cm^{-2}$ [27].

2.3. Structural characterization

High-resolution transmission electron microscopy (HR-TEM; FEI Talos F200 TEM) was used for attaining bulk microscopy, SAED, STEM-HAADF, BF, and lattice fringe spacings. EDAX Octane Elect detector connected to an FEI Quanta 400 ESEM was used for elemental mapping under an acceleration voltage of 20 kV with a 10-mm working distance. The morphology and surface structure of the electrocatalysts were imaged using a field emission scanning electron microscope (FESEM);



Scheme 1. Schematic of the synthesis route for $Co-(NiFe)N@NiS_x@NF$ oxynitrides.

FEI/ThermoScientific ApreoS) typically under an acceleration voltage of 2 kV. The FESEM was equipped with an ETD and an in-lens Immersion detector. Specific surface areas of powder samples were obtained by applying the Brunauer-Emmett-Teller (BET) theory to N₂ adsorption-desorption isothermals using a Micrometrics ASAP 2020 at 77 K. Sample degassing conditions were set at 150 °C for 3 h at a ramp-up rate of 10 °C min⁻¹. Pore-size distributions were attained from the desorption branches using the Barrett-Joyner-Halenda (BJH) method. Crystallinity of the samples were determined using X-ray diffraction (XRD; Rigaku Ultima IV Multipurpose X-ray Diffractometer). The diffractometer was equipped with cross beam optics, a fixed monochromator, and a scintillation counter. The XRD radiation source (Cu-Kα) was operated at 40 kV and 40 mA. A divergence slit (2/3°), divH.L. Slit (10 mm), scattering slit (2/3°), and a receiving slit (0.3 mm) were used. The XRD data were collected using continuous scan mode in the 2θ range of 5–80° with step width of 0.02° and 0.5°/minute scan speed. X-ray Photoelectron Spectroscopy (XPS; AXIS Ultra DLD) was applied to collect a large area survey and high-resolution X-ray photoelectron spectra of the oxynitride samples. The XPS Al mono (K-alpha) radiation (1486.6 eV) source was operated at 15 kV and 15 mA emission current. The high-resolution spectra of Cobalt 2p, Nickel 2p, Iron 2p, Sulfur 2p, Nitrogen 1 s, and Oxygen 1 s peaks were collected with a pass energy of 20 eV and 0.1 eV step size. The XAS signal was collected by Vortex detector in 9BM beamline of Advanced Photon Source (APS) in Argonne National Laboratory. X-ray absorption near-edge spectra (XANES) of Co and Fe K-edge were collected by silicon drift detector at ambient air in 9BM beamline of Advanced Photon Source (APS) located in the Argonne National Laboratory.

2.4. Electrochemical measurements

All electrochemical measurements were performed in a customized three-electrode configuration electrochemical cell, whereby the NF-based catalyst acts as the working electrode, a saturated calomel electrode (SCE) as the reference electrode ($E_{\text{Ag/AgCl}}^0 = 0.242$ V) for neutral pH electrolytes, an Ag/AgCl (sat. KCl) as the reference electrode ($E_{\text{Ag/AgCl}}^0 = 0.197$ V) for alkaline conditions, and a graphite rod as the counter electrode. Both cyclic voltammetry (CV) and linear sweep voltammetry (LSV) polarization measurements were undertaken using a Gamry Reference 3000 electrochemical workstation. LSV polarization data were recorded at a scan rate of 5 mV s⁻¹ and a step size of 2 mV irrespective of the electrolyte. CV polarization data were recorded at the same step size, but at slower scan rates of 1 mV s⁻¹. All polarization data are displayed relative to the reversible hydrogen electrode (RHE) in accordance to $E_{\text{RHE}} = E_{\text{Ref}} + 0.059 \text{ pH} + E_{\text{Ref}}^0$, where E_{Ref}^0 equals 0.242 V for SCE and 0.197 V for Ag/AgCl as reference electrodes. Tafel slopes (b) were obtained through fitting the linear regions of the Tafel plots using the Tafel equation ($\eta = b \log(j) + a$), where η is the overpotential in mV, j is the current density in mA cm⁻², and b is the Tafel slope in mV dec⁻¹. The overpotential (mV) region used to determine the Tafel slope corresponds to a current density range between 2 and 10 mA cm⁻² such that mass-transport limitation effects are minimized on porous NF substrate. Before collecting LSV, current stabilization was ensured by performing ~5 cycles of CV. The uncompensated solution resistances (R_s) were determined using Nyquist plots from electrochemical impedance spectroscopy (EIS) measurements, and the obtained values were used for performing 90% iR corrections on the respective LSV polarization curves. Charge transfer resistance (R_{CT}) of each catalyst relative to the working electrolyte was obtained from fitting the same Nyquist plots, which were obtained from EIS measurements at 1.55 V vs. RHE in the frequency range of 1 MHz to 1 Hz and an amplitude AC voltage of 10 mV. Electrochemical stability was ascertained through chronoamperometry (CA) measurements, through which the potential is fixed to correspond to a desired current density, and the attained current density with respect to time is constantly recorded. The electrochemical surface area (ECSA) was approximated through the double-layer

capacitance (C_{dl}) values obtained in the non-Faradaic potential range of 1.1–1.2 V (vs. RHE), in which the Faradaic reaction cannot be observed, at increased CV scan rates from 20 to 160 mV s⁻¹. The ECSA is proportional to C_{dl} based on the equation $\text{ECSA} = C_{\text{dl}}/C_s$, whereby C_s in the alkaline electrolyte is approximately a constant (0.04 mF cm⁻²) [27, 31]. To probe both alkaline and neutral pH performance of the Co-(NiFe) N based electrocatalysts in saline waters, a parametric study was conducted on different saline (0.6 M NaCl) and synthetic seawater electrolytes. FE calculations for OER versus CER selectivity were conducted through on-line gas chromatography (GC) measurements of oxygen concentration at known time intervals during electrochemical CA stability tests. The theoretical moles of oxygen ($n_{\text{O}_2, \text{theory}}$) is calculated at a recorded sample time and current " I (A)" through $n_{\text{O}_2, \text{theory}} = I/zF$; where $z = 4$ represents the electrons transferred per ion and $F = 96485.2 \text{ s A mol}^{-1}$ represents the Faradaic constant. Further, at measured volumetric flowrate of helium as carrier gas (" V_{He} (m³ s⁻¹)", the moles of helium " n_{He} " are calculated under ideal gas law assumption ($n_{\text{He}} = V_{\text{He}}P/RT$; where $P = 101325 \text{ Pa}$ represents pressure, $R = 8.314 \text{ kg m}^2 \text{ s}^{-2} \text{ mol}^{-1} \text{ K}^{-1}$ is the ideal gas constant, and $T = 293 \text{ K}$ is the temperature). The theoretical oxygen concentration " $C_{\text{O}_2, \text{theory}}$ " is then calculated as $C_{\text{O}_2, \text{theory}} = n_{\text{O}_2, \text{theory}}/(n_{\text{He}} + n_{\text{O}_2, \text{theory}})$ and the FE (%) is acquired from the ratio between GC-recorded O₂ concentration and by $C_{\text{O}_2, \text{theory}}$. Calibration of the GC was performed by measuring known O₂ concentrations (i.e., 1%, 2%, and 4% in He balance).

3. Results and discussion

3.1. Synthesis and electrocatalyst structure

Synthesis of Co-(NiFe)N @ NiS_x@NF entailed three steps, as shown in Scheme 1. First, hydrothermal sulfurization was utilized to grow a homogenous layer of NiS_x atop the underlying porous NF. Confirmation of this was ensured through several analyses including XRD, Raman, and FESEM. The latter textural characterization technique was employed alongside elemental mapping on a freshly synthesized piece of NiS_x@NF. As can be seen from Fig. 1a, the triangular shaped piece intentionally etched off the NiS_x@NF prior to characterization shows a clear thickness difference along the NF. Further, elemental mapping of this area confirms lack of NiS_x in the etched region and a homogeneously distributed NiS_x@NF surface on the electrode. Subsequent to growth of NiS_x, the Co-(NiFe) precursor was grown directly atop NiS_x@NF, or on pre-treated NF in the case of Co-(NiFe)N @ NF. The as-fabricated layered Co-(NiFe) catalytic oxide was then nitrated through a urea-assisted mechanism in a programmable tubular furnace adapted from our previous work [32]. The NH₃ produced from urea decomposition acts as both the reducing and nitrating source in this mechanism, effectively enabling the formation of a homogenous distribution of nitride character along the surface of the Co-(NiFe)N @ NiS_x@NF which exhibits oxide character from the preceding hydrothermal and thermal treatment under the nitridation step.

Surface morphologies and elemental mapping of both the non-sulfurized and sulfurized samples are presented in Figs. 1b and 1c, respectively. As can be seen, the morphologies are quite different whereby the NiS_x interlayered surface in Fig. 1c displays a qualitatively larger surface area than the more laminar Co-(NiFe)N @ NF surface morphology shown in Fig. 1b. This is further showcased through BET analyses in Fig. S1a which resulted in calculated BET surface areas of 44.7 and 172.9 m² g⁻¹, and BJH average macropore sizes of 53.1 and 44.9 nm for Co-(NiFe)N @ Ni and Co-(NiFe)N @ NiS_x @Ni, respectively. High BET surface areas (> 40 m² g⁻¹) have been reported for bimetallic oxides previously [33], which have been directly correlated to improved electrochemical performance due to enhanced kinetics. Attaining large pore sizes is considered advantageous for facile elimination of generated gases during electrolysis. Although further work is needed to confirm the direct source of enhanced pore size, it is potentially from the nitridation step both samples undergo. Furthermore,

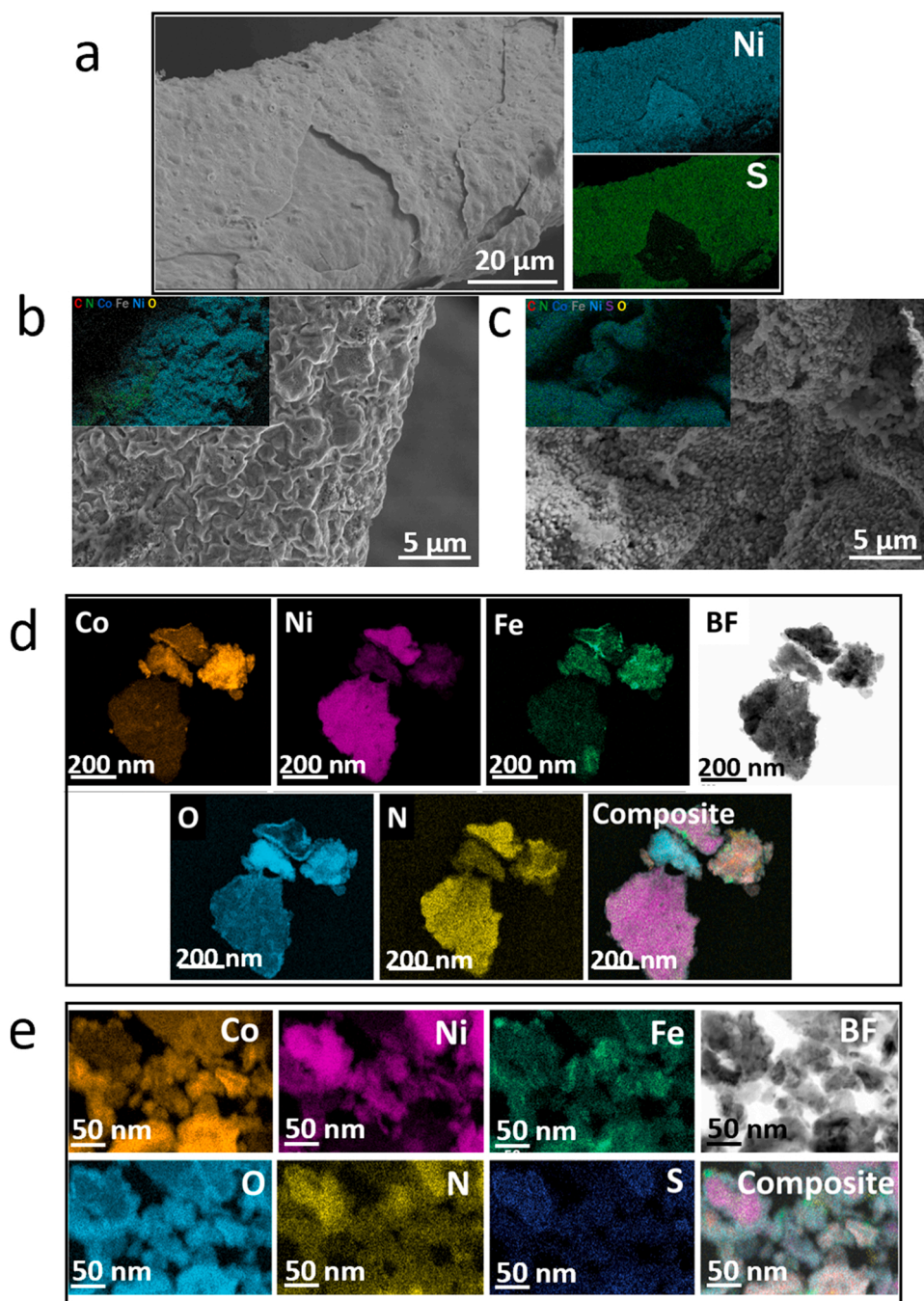


Fig. 1. (a) FESEM image and corresponding elemental mapping of NiS_x@NF, (b) FESEM image and corresponding composite elemental map of as-prepared Co-(NiFe)N @ NF and (c) Co-(NiFe)N @ NiS_x@NF. (d) Color-coded HRTEM elemental maps and Bright Field (BF) images of as-prepared Co-(NiFe)N @ NF and (e) as-prepared Co-(NiFe)N @ NiS_x@NF. Color-coded elemental maps correspond to Co (orange), Ni (magenta), Fe (green), O (cyan), N (yellow), and S (purple).

Table S1 notes that the attained average particle sizes for the non-interlayered and NiS_x interlayered samples were 134.2 and 34.7 nm, respectively, which are in good agreement with representative particles showcased in HRTEM images presented in Figs. 1d and 1e. Larger scan (lower magnification) regions of both materials are presented in Fig. S2 along with the corresponding EDS spectra for confirming purity and homogenous elemental presence on the surface. Fig. S2a for Co-(NiFe)N @ NF exhibits several regions of localized nitridation, appearing in green, unlike Co-(NiFe)N @ NiS_x@NF in Fig. S2b. This is further confirmed from bulk HRTEM elemental maps taken for both electrocatalysts shown in Figs. 1d and 1e. HRTEM elemental mapping of Co-(NiFe)N in Fig. 1d clearly shows localized

deposits of Co and Fe oxides, and Ni nitrides whereby clearcut phase separation is evident. Typically phase separation is disadvantageous towards electrocatalytic activity [34] and more importantly it is not intended for our electrocatalyst design rationale whereby neighboring surface sites of metallic oxides and nitrides are effectively hetero-interfaced. Presence of the NiS_x interlayer in the sulfurized sample is apparently indicative of a more homogenized favorable bulk elemental distribution, as shown in Fig. 1e. It is important to note that both Co-(NiFe)N @ Ni and Co-(NiFe)N @ NiS_x@Ni samples that underwent HRTEM analysis are powder in nature, and therefore the Ni NPs used as growth substrate show up on the elemental mapping scans in Figs. 1d and 1e with a higher intensity. This may misleadingly present a case

where localized Ni is found present on both samples, suggesting a non-homogenous distribution of elements on both samples. However, the uniform distribution of Co, Fe, O, N, and S elements on the interlayered Co-(NiFe)N @ NiS_x @ Ni in Fig. 1e confirms the homogenization of elements herein, relative to Co-(NiFe)N @ Ni in Fig. 1d. Further, presence of all anionic components (i.e., O²⁻, N³⁻, and S²⁻) is confirmed in the sampled area, and with apparent bonding to all cationic components (Co²⁺, Ni²⁺, and Fe²⁺) suggesting no clear phase separation phenomena. Moreover, the same surface textural characterization was performed on both samples after OER operation in neutral pH SSW (1 M PB + 35 g/L SSW). This analysis was performed to determine whether any morphological changes to the catalytic surfaces occurred during OER in seawater electrolyte. Figs. S2a and S2e show clear increases in exposed surface areas through subtle surface morphological transformation into nanosheets and nanorods for Co-(NiFe)N @ NF and Co-(NiFe)N @ NiS_x@NF, respectively. Elemental mapping and EDS analyses in Figs. S3b-d on Co-(NiFe)N @ NF exhibits presence of surface retained Cl⁻ and leaching of metallic Ni and Fe during OER in SSW electrolyte.

This is contrary to what occurs on the NiS_x interlayered catalyst whereby surface adsorbed Cl⁻ was not detected (Figs. S3f-h), catalyst metals constituents were not leached, and homogenous elemental distribution is maintained post-OER. Visually, this was confirmed during electrochemical stability tests with Co-(NiFe)N @ NF whereby initial color change from clear to green occurred to electrolyte, followed by an increased light brown hue. The initial green spectra are from Ni²⁺ leaching, followed by Co²⁺ and Fe²⁺ which contribute to the light brown/reddish hue attained after a prolonged sustained operational time.

3.2. Textural and crystallinity regulation

Structure and composition of the as-prepared electrocatalysts were characterized through several textural techniques. Bulk HRTEM imaging of the Co-(NiFe) based oxynitride samples was performed to determine the crystal structure of the developed oxynitrides at the atomic scale. Figs. 2a and 2d display different magnification HRTEM of Co-(NiFe)

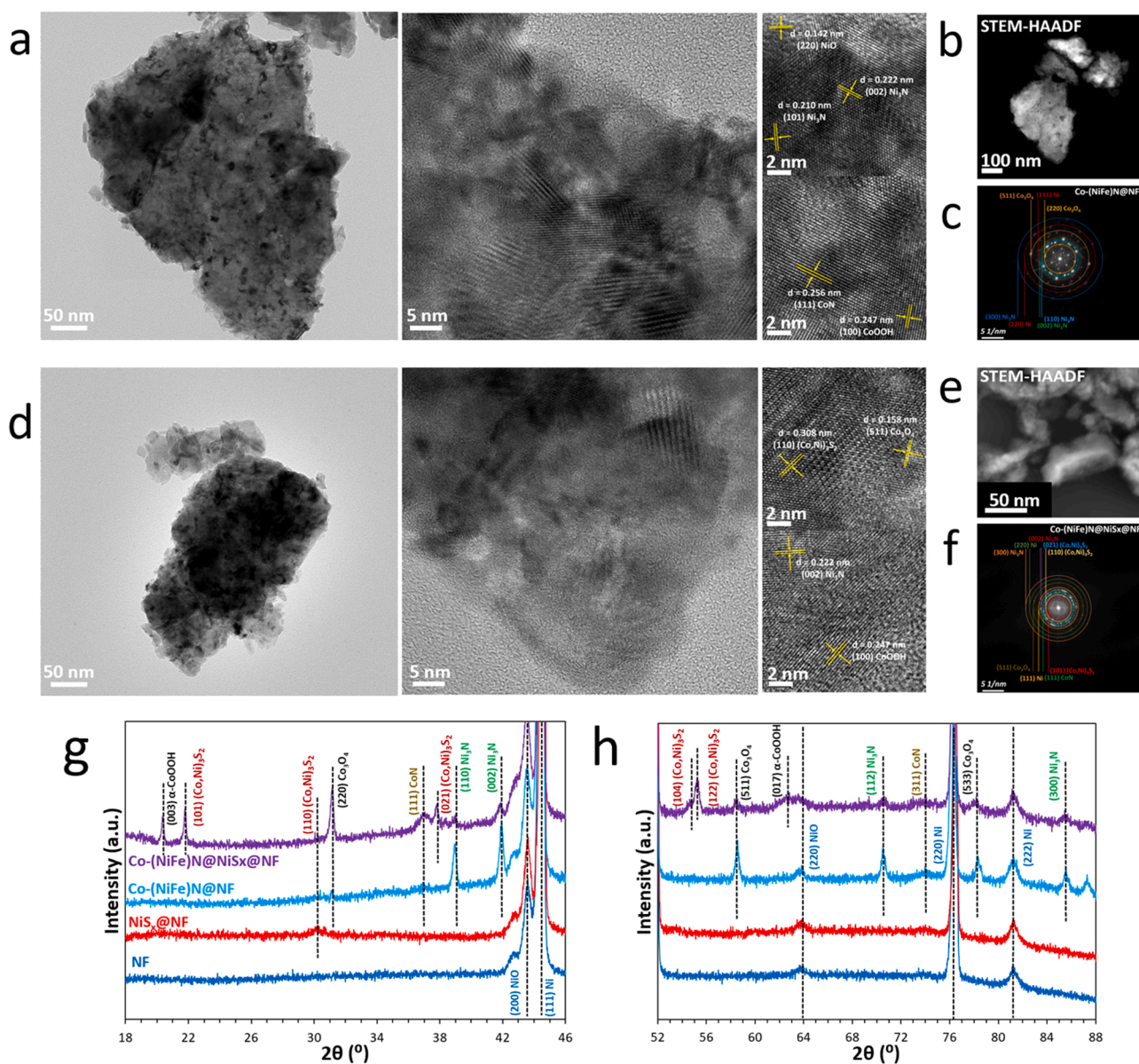


Fig. 2. (a, d) Different magnification HRTEM images (b, e) STEM-HAADF images, and (c, f) SAED patterns of Co-(NiFe)N @ Ni and Co-(NiFe)NiS_x @ Ni, respectively. Expels to the right of HRTEM images display lattice fringe spacing the respective as-prepared electrocatalysts. (g, h) Magnified XRD patterns of as-prepared electrocatalysts grown atop NF.

N @ Ni and Co-(NiFe)N @ NiS_x @ Ni, respectively. As can be inferred from the central expels of both Fig. 2a (Figs. S4) and 2d (Fig. S5), a smaller (~ 5 nm) quasi-amorphous surface thickness is noted for Co-(NiFe)N @ Ni in Fig. 2a, relative to the larger quasi-amorphous thickness (~ 10–20 nm) on the NiS_x interlayered sample (Co-(NiFe)N @ NiS_x @ Ni) in Fig. 2d. Lattice fringe determination on different regions of the samples strongly indicate a core-sheath like assembly, typical of electrocatalysts prepared through a hydrothermal-nitridation procedure [25]. This is further conveyed through presence of more crystalline Ni₃N (i.e., (002) Ni₃N, *d* = 0.222 nm) [35] phase further away from the sheath layer on both samples, and the anodically electroactive quasi-amorphous phase (i.e., (100) CoOOH [27] within the sheath layer. Of interest to the phase separation discussion, Fig. 2a for Co-(NiFe)N @ Ni shows a clear regional localization of Co and Ni-based phases, respectively, whereby *d* spacings of 0.142, 0.222, and 0.210 nm correspond to (220) NiO, (002) Ni₃N, and (101) Ni₃N, respectively in the right-most area of the imaged area, and *d* spacings of 0.256 and 0.247 nm for (111) CoN and (100) CoOOH [36], respectively, are on the left-most region of the same imaged area. This is contrary to the distribution of phases found for the Co-(NiFe)N @ NiS_x @ Ni sample in Fig. 2d, whereby a more uniform distribution of Co and Ni-based phases are found throughout the sampled region. Although interlayered sulfurization was not expected to be probed through HRTEM, *d*-spacings of 0.308 nm were attributed to (110) (Co,Ni)₃S₂ in Fig. 2d, which are slightly larger than reference (110) Ni₃S₂ *d*-spacing of 0.287 nm [37]. However, the difference is believed to be due to lattice expansion from larger radii cobalt relative to nickel atoms in the lattice. This suggests that during the hydrothermal layered oxidation and final nitridation steps, initial sulfurized character propagates to the surface and potentially binds with surface metallic constituents. The importance of this nanoscale effect on catalytic performance can best be conveyed through rationalizing neighboring Co and Ni-based oxide and nitride sites with varying binding energies for H₂O dissociation and OER intermediates propagation. Increasing the geometric surface distance between such active sites may result in OER intermediates binding strongly to unfavorable sites without the ability to facilitate propagate to the next mechanistic step, effectively lowering the already limited kinetics in neutral pH regimes [38].

Scanning transmission electron microscopy (STEM) high-angle annular dark-field (HAADF) imaging was performed on Co-(NiFe)N @ Ni and Co-(NiFe)N @ NiS_x @ Ni in Figs. 2b and 2e, respectively, and a more homogenous contrast in Fig. 2e further confirms the phase homogeneity of the NiS_x interlayered sample. Selected area electron diffractograms (SAED) in Figs. 2c and 2f corroborate *d*-spacings indexed from HRTEM imaging, and crystallinity parameters of SAED and *d*-spacings corroborate those presented in XRD patterns of Fig. 2 g and 2 h for the as-prepared electrocatalysts. Wide-angle XRD through diffractograms attained from the as-prepared electrocatalysts on NF are presented in Fig. S6a. Due to the larger presence of NF character, it is difficult to determine whether clear phases of Co, Ni, and Fe are indeed present on the NF substrate without magnification and low-scan rate (0.5°/minute) measurements undertaken. Higher resolution XRD data for 2θ between 18 and 46° and 52–88° are presented in Fig. 2 g and 2 h, respectively, for the as-prepared surface heterointerfaced oxide/nitride electrocatalysts and NiS_x@NF and NF as controls. Although only the (110) metallic sulfide peak is present in NiS_x@NF control sample, Co-(NiFe)N @ NiS_x@NF exhibits several (Co,Ni)₃S₂ peaks corresponding to the (101), (110), (021), (104) and (122) facets. This suggests that upon hydrothermal growth of Co-(NiFe) and subsequent heat treatment from nitridation, pre-existing sulfurized character propagates and rearranges on the surface in (Co,Ni)₃S₂ phase. Presence of the same (Co,Ni)₃S₂ hexagonal phase (JCPDS No. 44-1418) was also confirmed through SAED and lattice fringe measurements of the same catalyst [39]. Furthermore, nitride character is predominantly found as the Ni₃N phase (JCPDS No. 10-0280) for both Co-(NiFe)N and Co-(NiFe)N @ NiS_x, although (111) and (311) CoN (PDF No. 83-0831) peaks were

also attained. In congruence with the larger quasi-amorphous sheath layer on the NiS_x interlayered catalyst, clear (003) and (017) α-CoOOH facets (JCPDS No. 73-1212) [40] are present for the Co-(NiFe)N @ NiS_x@NF sample. Furthermore, in an effort to identify active phases on Co-(NiFe)N @ NiS_x@NF, XRD analysis was performed on control samples of Co-(Ni)N @ NiS_x@NF, Co-(Fe)N @ NiS_x@NF, and (NiFe)N @ NiS_x@NF as shown in Fig. S7. First, metal sulfide peaks are consistently present on all control samples, confirming successful incorporation of top catalytic layer atop NiS_x@NF. In the absence of Co or Ni, (220), (331), and (440) Fe₃S₄ phases (JCPDS 89-1998) are apparent, suggesting that sulfide character incorporates with Fe, albeit to a small degree. In (NiFe)N @ NiS_x@NF, the absence of Co allows for a notable increase in favorable Ni-LDH character known for effectively oxidizing OH⁻ under alkaline electrolyte. For the same sample, nitride character is also prominent, as it is for other Ni-containing samples. Nevertheless, Co-(Fe)N @ NiS_x@NF does exhibit notable (111) CoN and (110) Fe₃N peaks, confirming surface nitridation. These findings become increasingly important in identifying the active roles that different phases play under different electrolytic environments, as will be discussed in Section 3.4.

Raman analysis in Fig. S6b was also undertaken on the prepared sample along with a control Co-(NiFe)O@NiS_x@NF sample to deconvolute oxide from nitride character. Tetrahedral Co²⁺ (3d⁷) and octahedral Co³⁺ (3d⁶) in spinel Co₃O₄ exhibit a characteristic vibrational mode at 456 cm⁻¹ in the control Co-(NiFe)O@NiS_x@NF sample [41], which is significantly diminished upon nitridation. Similarly, NiO peak around 543 cm⁻¹ in the same control sample is broadened upon nitridation, suggesting strong interactions occurring between Co/Ni/Fe during oxide to nitride transition. Confirmation of nitride character is shown by the 470 cm⁻¹ peak in Co-(NiFe)N @ NiS_x@NF corresponding to cubic CoN phase. This can be explained through the desired heterointerfaced character upon nitridation. Characteristic Ni-S bonds are confirmed in both the control NiS_x@NF and Co-(NiFe)N @ NiS_x@NF samples, whereby both Ni-S (i.e., E_g (250 cm⁻¹) and E_g (306 cm⁻¹)) and Co-S vibration modes are clearly apparent in the Co-(NiFe)N @ NiS_x@NF. Postmortem crystallinity characterization through XRD analysis on Co-(NiFe)N @ NiS_x@NF is presented in Fig. S8 and clear phase transformation away from crystalline metal sulfide peaks is shown between the two spectra.

3.3. Spectroscopic analysis of NiS_x on Co-(NiFe) valence regulation

For further characterization of the prepared surface oxide/nitride heterointerfaced structures, an X-ray absorption fine structure (XAFS) analysis at the Co and Fe K-edges was performed. Reference spectra for spinel cobalt oxide (Co₃O₄; Co²⁺/Co³⁺), monoclinic CoO (Co²⁺), metallic Co foil (Co⁰), iron oxide (Fe₂O₃; Fe³⁺), and metallic Fe foil (Fe⁰) were used in Fig. 3. Furthermore, an oxide-based Co-(NiFe)O_x @ NiS_x @ Ni sample was prepared and used as a control to investigate the effect of the sulfide interlayer. The oxidation state of Co and Fe in the samples were determined by interpolation of a linear relationship between the XANES absorption edge (Figs. 3a and 3d) and the theoretical oxidation state of the control samples (Figs. 3b and 3e). Absorption edge positions in Figs. 3b and 3e were determined from XANES by mathematically obtaining inflection points in the spectral jumps through calculating and plotting the second derivatives of respective XANES spectra and correlating the x-intercepts with phonon energies. We found that the as-prepared electrocatalysts exhibited a lower Co oxidation state for the NiS_x interlayered sample. As reported in our recent work and through density-functional theory (DFT) calculations by Bajdich et al., the Co²⁺/Co³⁺ transition is more thermodynamically favorable relative to Co³⁺/Co⁴⁺ [42]. Thus, having Co^{δ+} with *δ* closer to 2 is favored for OER, which is the case in the NiS_x interlayered sample. This comes with a tradeoff with respect to the oxidation state for Fe, whereby a higher oxidation state for Fe was attained for the NiS_x interlayered sample, suggesting a regulating effect Fe plays on Co^{δ+} during oxidation to

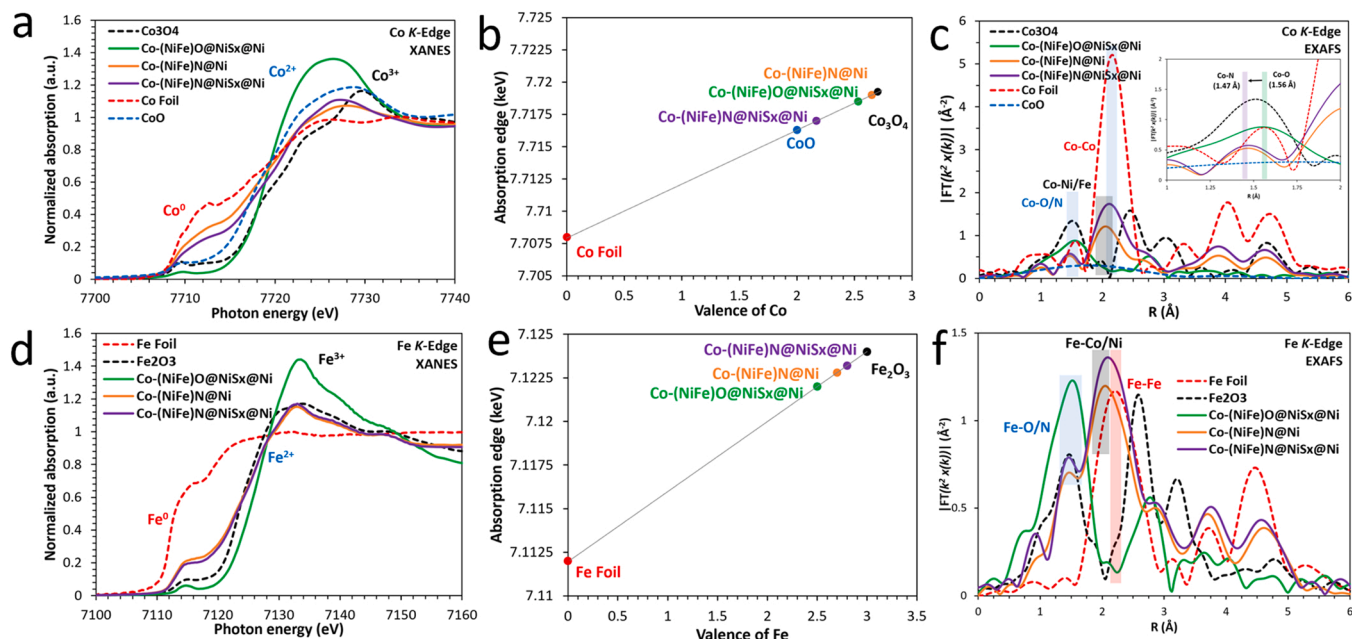


Fig. 3. (a, b, c) Co K-edge XANES, attained Co valence, and EXAFS Co K-edge of as-prepared Co-(NiFe)N @ Ni, Co-(NiFe)N @ NiS_x @ Ni, Co-(NiFe)O@NiS_x @ Ni, and reference Co materials. (d, e, f) Fe K-edge XANES, attained Fe valence, and EXAFS Fe K-edge of as-prepared Co-(NiFe)N @ Ni, Co-(NiFe)N @ NiS_x @ Ni, Co-(NiFe)O@NiS_x @ Ni, and reference Fe materials.

maintain active site Co^{δ+} closer to the desired Co²⁺. Moreover, the extended x-ray-absorption fine-structure (EXAFS) for both Co- and Fe-edge in Figs. 3c and 3f, respectively, showed that a convolution of metallic Co-Co, Co-Ni/Fe, Fe-Fe, and Fe-Co/Ni character are present in Co-(NiFe)N-based electrocatalysts and their complete absence in the Co-(NiFe)O counterparts. The corresponding interatomic distances for Co-Co and Fe-Fe are slightly lower than the reference Co⁰ and Fe⁰ foils in Figs. 3c and 3f, respectively, potentially due to lattice strains around Co⁰/Fe⁰ nanoclusters from neighboring Ni, Co, and Fe. Importantly, EXAFS analysis confirms the standard difference between both cobalt

oxide and nitride characters present on the surface, whereby interatomic distances of 1.56 and 1.47 Å for Co-O and Co-N, respectively, are clearly present in the inset of Fig. 3c for Co-(NiFe)N-based samples.

XPS analysis on Co-(NiFe)N @ NF and Co-(NiFe)N @ NiS_x@NF samples to elucidate the chemical valence of the oxyhydrides as-prepared (pre-OER) and after neutral pH SSW OER (post-OER) to investigate surface chemical changes under the oxidative environment during operation. Full-range XPS spectra displayed in Fig. S9a verify Co, Ni, Fe, O, N, and S (for the NiS_x interlayered sample), with no residual impurities from synthesis steps. Prior to high-resolution elemental spectra

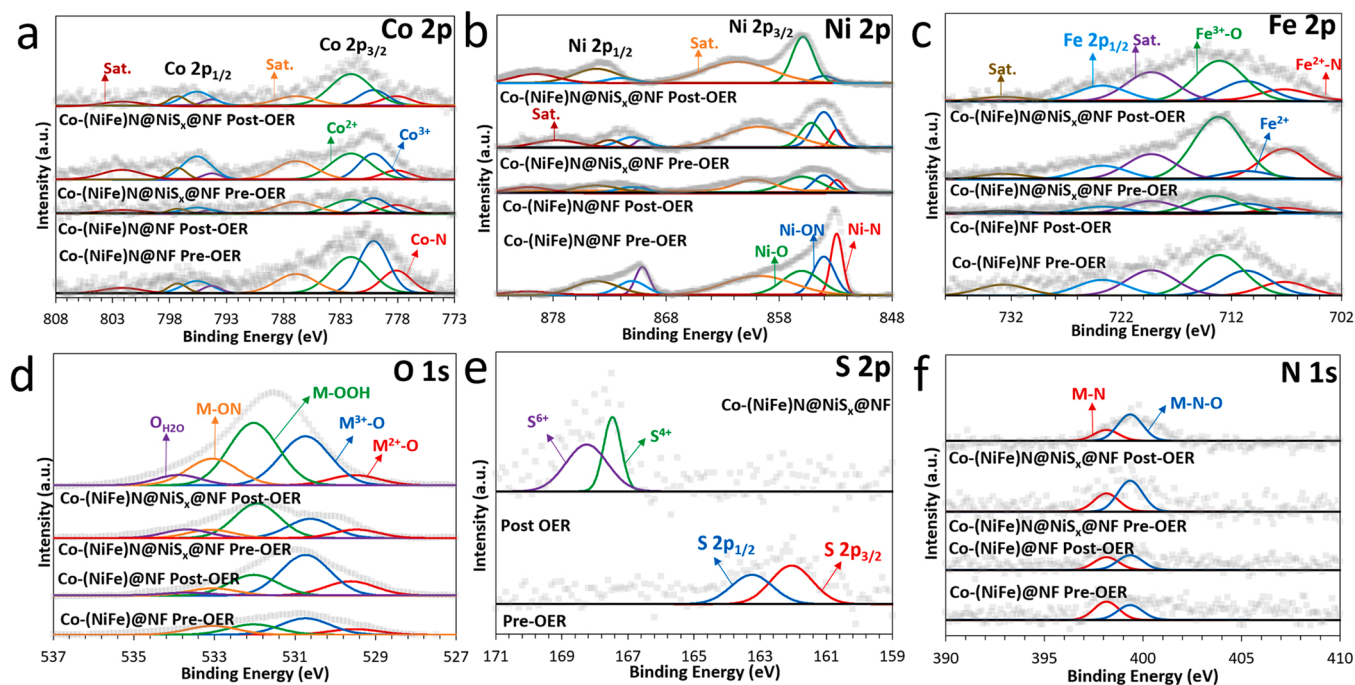


Fig. 4. (a) High-resolution XPS spectra of Co 2p, (b) Ni 2p, (c) Fe 2p, (d) O 1s, (e) S 2p, and (f) N 1s for Co-(NiFe)N @ NF and Co-(NiFe)N @ NiS_x@NF before and after 24-hours OER in neutral pH SSW.

deconvolution, the raw spectra was subtracted through the Iterated Shirley background subtraction method, shown in Fig. S9b [27]. Fig. 4a highlights the high-resolution Co 2p XPS spectra for the aforementioned samples and notable Co^{3+} and Co^{2+} $2p_{3/2}$ at binding energies of 780.2 and 781.9 eV are present in all samples [27]. Both as-prepared and post-OER Co 2p spectra for Co-(NiFe)N @ NiS_x @NF exhibit a larger $\text{Co}^{2+}/\text{Co}^{3+}$ ratio relative to the Co-(NiFe)N @ NF sample suggesting a regulating effect from dopant elements that allow more thermodynamically favorable lower oxidation states for Co-based active sites in the NiS_x interlayered sample. As noted previously in XAS discussion, a larger degree of Co^{2+} accelerates the rate-determining third electron-transfer step ($\text{M-O} + \text{OH}^- \rightarrow \text{M-OOH} + \text{e}^-$) in the conventional adsorbate evolution mechanism (AEM) for OER. This is due to cycling through the $\text{Co}^{3+}/\text{Co}^{4+}$ transition is the thermodynamic-limiting step and the larger contributor to OER overpotential, whereas surface oxidation state manipulation towards a lower valence $\text{Co}^{2+}/\text{Co}^{3+}/\text{Co}^{4+}$ enables lower overpotential [42]. Peaks centered at 787.6 and 803.7 eV correspond to satellite peaks which convey the mixed valence of the oxynitride character in the as-prepared samples. The Co-N character is confirmed in all samples at peak location 778.2 eV, and high concentrations are particularly present in the as-prepared Co-(NiFe)N @ NF sample suggesting higher localized Co-N character [43], as well as Ni-N character (852.8 eV in Fig. 4b) [44] for the same sample, as suggested by HRTEM elemental maps previously in Section 3.2. The aforementioned metal-nitride character is partially beneficial as it is known to enhance the electrical conductivity in electrocatalysts and facilitate rapid electron transport, which is fundamentally significant in kinetically challenging electrolytic conditions. Moreover, peak deconvolution of Ni 2p spectra in Fig. 4b exhibits Ni-O-N and Ni-O_x peaks shifted from their standard peak positions to binding energies of 854.1 and 855.8 eV, respectively, whereby for example the former is negatively shifted from the standard Ni-O-N peak positions of 855.5 eV by 1.4 eV [25,45]. The as-prepared Co-(NiFe)N @ NiS_x @NF exhibits a notably higher ratio of oxynitride character relative to the predominant Ni-N character in Co-(NiFe)N @ NF. Further, negative shifting in the Ni-O-N peak suggests synergistic surface heterojunction and consequent electron delocalization and thus electron transport from lower electronegativity Ni to neighboring Co (favoring higher $\text{Co}^{2+}/\text{Co}^{3+}$ ratio) and $[\text{O-N}]^{\delta-}$. Upon OER, Ni-(OOH) or Ni-(OH)₂ character in both electrocatalyst increases as expected, however this predominates the Ni 2p spectra in the post-OER Co-(NiFe)N @ NiS_x @NF catalyst suggesting electroactive Ni-based sites during OER. Similarly, the fitted Fe 2p spectra shows the expected Fe-N, Fe^{2+} , and Fe^{3+} oxide-based peaks at binding energies of 706.9, 710.4, and 713.2 eV, respectively [46]. High Fe^{3+} concentration in the post-OER samples confirms the regulating and synergistic effect among Ni, Co, and the electron-dense anionic oxynitride character. The apparent dissolution or leaching of metallic character post-OER for the Co-(NiFe)N @ NF electrocatalyst that was detected by the FESEM elemental mapping shown in Fig. S3, is confirmed by the decreases in the spectral areas of Co 2p, Ni 2p, and Fe 2p shown in Fig. 4a-c for the same post-OER sample.

Peak positions in the O 1s spectra in Fig. 4d corresponding to different lattice oxygen (i.e., $\text{M}^{2+}\text{-O}$ and $\text{M}^{3+}\text{-O}$), oxyhydroxide character (M-OOH), heterojunctioned oxide/nitride or oxynitride features (M-O-N), and chemisorbed H₂O corroborate the aforementioned transformation from predominantly lattice oxygen to oxyhydroxide/oxynitride character upon OER. Of particular note, the M-OOH and M-O-N peaks around 532.1 and 533.1 eV, respectively [25], can be deconvoluted further for the Co-(NiFe)N @ NiS_x @NF sample to include surface bound SO_4^{2-} character around 532.3 eV from the transformation of the NiS_x to polyanionic sulfate and sulfite species during OER. The transformation from lattice terminal and central polysulfide character at 162.1 (S $2p_{3/2}$) and 163.4 eV (S $2p_{1/2}$), respectively, to surface bound SO_3^{2-} and SO_4^{2-} is further confirmed from the postmortem-OER Co-(NiFe)N @ NiS_x @NF spectra in Fig. 4e, whereby S^{4+} and S^{6+} characters in the latter sample correspond to SO_3^{2-} and SO_4^{2-} , respectively [47]. This is in

good agreement with pre- and postmortem OER XRD analysis on the same catalyst highlighted in Fig. S8. A higher degree of adsorbed H₂O is apparent in the as-prepared Co-(NiFe)N @ NiS_x @NF suggesting better hydrophilicity which is important for neutral pH water oxidation where H₂O is the primary reactant. High-resolution N 1s spectra in Fig. 4f showcases M-N and M-N-O peaks around binding energies of 398.3 and 399.8 eV, respectively, with an increase in the M-N-O ratio after OER for both catalysts – albeit to a larger degree for the NiS_x interlayered sample [48]. Based on atomic percentages from survey scans in Fig. S9a, 3.83% and 3.95% atomic nitrogen is present on the surface of Co-(NiFe)N @ NF and Co-(NiFe)N @ NiS_x @NF, respectively, with atomic oxygen content being on average eight times more abundant on the surface. XRD data in Fig. 2 g and 2 h, and spectral deconvolution in Fig. 4 confirmed surface oxyhydroxides which have an oxygen to metal ratio of 2–1. Contrasting this with the predominant Ni_3N character (1–3 nitrogen to metal ratio), a metallic trivalent site will have on average 6 times more oxygen than nitrogen. The remaining makeup is potentially due to a high ratio of nitride character preferentially forming Ni_3N near Ni-based foam substrate. Homogenous surface heterojunctions between oxide/nitride character has been confirmed from HRTEM elemental mapping in Figs. 1d and 1e, as well as deconvolution data, particularly N 1s spectra in Fig. 4f. The surface heterointerfaced M-N-O structure can better dissociate H₂O in neutral pH electrolytes through sites of stronger and weaker binding energies towards H₂O intermediates (i.e., OH^- and H^+), thereby allowing hydroxides to propagate towards OER and repelling H^+ through weak binding energies.

3.4. Electrocatalytic performance

To probe the attained electrochemical performance towards OER in conventional alkaline pH media, both Co-(NiFe)N @ NF and Co-(NiFe)N @ NiS_x @NF were tested first in conventional alkaline water electrolyte (DIW + 1 M KOH). This electrolytic condition was also used for initial electrochemical screening purposes to optimize the electrocatalyst composition, whereby a 3, 4, and 5–1 ratio of Ni to Fe were fabricated and their electrocatalytic performance was tested for both the interlayered catalyst and the non-interlayered catalyst. As shown in Fig. S10a, the 3:1 ratio, dubbed Co-(NiFe)N @ NiS_x @NF-3, attained the highest activities. Similar electrochemical screening analysis done in neutral pH saline electrolyte (1 M PB + 0.6 M NaCl), and the results shown in Fig. S10b show that substantial activity enhancement was observed for the Co-(NiFe)N @ NF-3 and Co-(NiFe)N @ NiS_x @NF-3. These samples are the same samples that are referred to as Co-(NiFe)N @ NF and Co-(NiFe)N @ NiS_x @NF, respectively, throughout this work. Briefly, under alkaline non-saline conditions, both materials registered exceptionally high activities whereby the overpotential requirement for attaining a current density of 100 mA cm^{-2} were 300 and 280 mV for Co-(NiFe)N @ NF and Co-(NiFe)N @ NiS_x @NF, respectively. Nearly similar performance was also obtained when testing in alkaline saline (0.6 M NaCl), suggesting negligible effect of electrolytic Cl^- on performance during a simple sweep across the potential range of interest. Upon testing in alkaline synthetic seawater (SSW) electrolyte, precipitation of Mg and Ca hydroxides are centrifuged out, as is typically done. Under the latter alkaline SSW electrolytic environment, electrocatalytic activity of both samples decreased, potentially due to a combination of residual Mg/Ca precipitation on anodic surfaces and exacerbated poisoning effects from seawater constituents. However, as shown in Fig. 5a, the overpotential requirement for reaching 100 mA cm^{-2} of current density in alkaline SSW electrolyte were 422 and 350 mV for Co-(NiFe)N @ NF and Co-(NiFe)N @ NiS_x @NF, respectively. Fig. 5b shows cyclic voltammograms for the interlayered sample in different alkaline pH environments. Anodic pre-oxidation peaks at 1.06 and ~1.4 V (vs. RHE) and cathodic peak at ~1.0 and 1.25 V (vs. RHE) reflect a thermodynamically facile quasi-reversible $\text{Co}^{2+}/\text{Co}^{3+}$ and $\text{Ni}^{2+}/\text{Ni}^{3+}$ redox couples, respectively. This suggests the formation of $\text{Co}(\text{OH})_2$ which is consequently converted to Co^{3+} oxyhydroxide

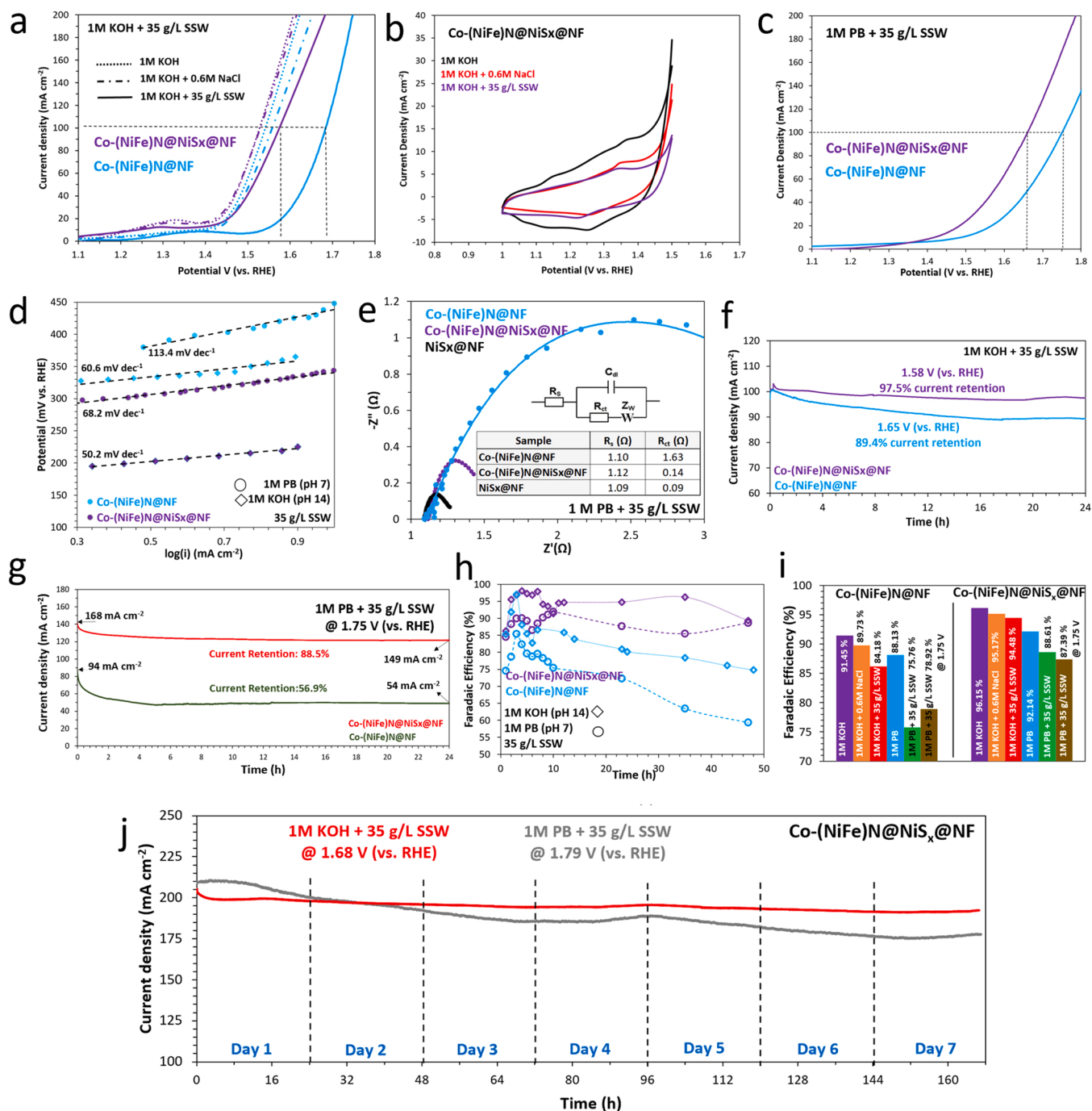


Fig. 5. (a) LSV polarization curves for Co-(NiFe)N @ NF and Co-(NiFe)N @ NiS_x@NF and (b) CV polarization curves of Co-(NiFe)N @ NiS_x@NF under different alkaline pH electrolytic conditions. (c) LSV polarization curves of Co-(NiFe)N @ NF and Co-(NiFe)N@NiS_x@NF under neutral pH synthetic seawater, (d) corresponding Tafel slopes under alkaline and neutral pH synthetic seawater, and (e) EIS Nyquist plots under neutral pH synthetic seawater. (f) Chronoamperometry stability curves at 100 mA cm⁻² of current density for Co-(NiFe)@NF and Co-(NiFe)@NiS_x@NF under alkaline synthetic seawater, (g) neutral pH synthetic seawater, and (h, i) corresponding Faradaic efficiencies under these conditions. (j) 7-days 200 mA cm⁻² CA study on Co-(NiFe)N @ NiS_x@NF under pH 14 and 7 SSW.

during OER, and similarly Ni²⁺ is oxidized to Ni³⁺ oxyhydroxide. Moreover, pre-oxidation of sulfide (S²⁻) around 1.145 V (vs. RHE) to SO₄²⁻ is also noted [49], which by design serves to enhance hydrophilicity, activity, and OER selectivity. The effect of sulfate to electrostatically shield the catalyst surface from Cl⁻ corrosive attack and the undesired CER has also been recently investigated and corroborated [50].

As noted earlier, amongst the several practical advantages that present themselves towards neutral pH seawater electrolysis is that the precipitation of Mg²⁺ and Ca²⁺ salts can be suppressed, advertently

enhancing the performance durability of both electrocatalysts and electrolyzer membranes [51]. Motivated by this, the designed Co-(NiFe)N @ NiS_x@NF electrocatalyst aimed towards facilitating facile H₂O dissociation under kinetically limiting neutral pH environments, whilst ensuring high FE towards OER over CER in saline waters. Fig. 5c showcases the attained polarization curves for both Co-(NiFe)N @ NF and Co-(NiFe)N @ NiS_x@NF in potassium phosphate buffered (pH 7) SSW electrolyte. The resultant overpotentials to reach a current density of 100 mA cm⁻² under these conditions were recorded at 523 and 425 mV for Co-(NiFe)N @ NF and Co-(NiFe)N @ NiS_x@NF,

respectively. Based on this metric alone, the developed electrocatalysts exhibit amongst the highest recorded activities for neutral pH OER to date. However, typical electrocatalyst development towards seawater electrolysis is performed under alkaline seawater, or SSW, conditions. For instance, contemporary NiFeN@NiMoN@NF [20], GO@Fe@Ni-Co@NF [52], and NiCoP/NiCo [53] required 307, 247, and 350 mV of overpotential at 100, 50, and 50 mA cm^{-2} , respectively, under alkaline SSW. This compares well with the 300 and 280 mV overpotential requirement for reaching 100 mA cm^{-2} of current density using the developed Co-(NiFe)N@NF and $\text{Co-(NiFe)N@NiS}_x\text{@NF}$ under the same conditions, as shown in Fig. 5a. Cheng et al. CoFe LDH fabricated attained 10 mA cm^{-2} under 530 mV of overpotential in synthetic seawater (pH 8) [54]. However, comparison with performances in neutral pH SSW was found difficult due to the majority of seawater electrolysis work being dedicated to alkaline electrolytes to make use of the Pourbaix diagram's alkaline design criteria in enhancing OER selectivity. Nevertheless, comparing activities with contemporary OER electrocatalysts in neutral pH (1 M PB) environments, NiCoP [55], Cu-CoP [56], and $\text{Co}_9\text{S}_4\text{P}_4$ [57] required overpotentials of 560, 411, and 570 mV to attain 10, 10, and 26 mA cm^{-2} of current density, respectively. These activities are well below that of 523 and 425 mV of overpotential required for sustaining 100 mA cm^{-2} of current density using the Co-(NiFe)N@NF and $\text{Co-(NiFe)N@NiS}_x\text{@NF}$ electrocatalysts developed in this work, respectively, under the more challenging neutral pH SSW conditions. In an effort to shed light on the kinetic regimes of the developed anodes, Tafel slopes were calculated from LSV polarization curves under alkaline and neutral pH SSW conditions. As can be seen in Fig. 5d, significantly faster kinetics indicated by lower Tafel slopes are present for the NiS_x interlayered sample. Of interest to neutral pH electrolysis, a low Tafel slope of 68.2 mV dec^{-1} under neutral pH SSW suggests that H_2O dissociation is not the rate-determining step (RDS). This is also the case for Co-(NiFe)N@NF , whereby the attained Tafel slope under the same neutral pH SSW conditions is below the 120 mV dec^{-1} , noted for the first step (H_2O dissociation) being the RDS. This finding suggests that the heterointerfaced design strategy of having surface charge delocalization from electron deficient (Co , Ni , Fe) $^{2+}$ and electron withdrawing (O , N) $^{\delta-}$ is effective at ensuring more kinetically facile H_2O dissociation. Further, in the presence of the NiS_x interlayer, the Tafel slope decreases significantly. This may be partially attributed to the enhanced hydrophilicity of the sample during OER, whereby surface SO_4^{2-} groups within the quasi-amorphous oxynitride character is known to enhance hydrophilicity [27,28].

BET- and ECSA-specific current density normalization were performed to probe the superior performance of $\text{Co-(NiFe)N@NiS}_x\text{@NF}$ relative to Co-(NiFe)N@NF . BET-normalized polarization curves in Fig. S11a in alkaline SSW electrolyte showcases a higher specific current density for the non-interlayered Co-(NiFe)N@NF relative to $\text{Co-(NiFe)N@NiS}_x\text{@NF}$ at increasing current densities. Lower BET-specific onset overpotential for $\text{Co-(NiFe)N@NiS}_x\text{@NF}$ confirms the higher intrinsic activity of the surface. However, kinetic limitations from surface bound polyanionic sulfates seemingly lowers diffusion of reactant OH^- to the Co-(NiFe)N surface which in effect results in a more sluggish current response at increasing potentials. To test this hypothesis, the same normalization was applied to polarization curves attained under alkaline saline (1 M KOH + 0.6 M NaCl) electrolyte, as shown in Fig. S11a. The same behavior is witnessed suggesting the lower activity is not due to electrode degradation, but is due to complete sulfide oxidation and leaching. Upon ECSA determination through the double-layer capacitance method (Figs. S11b-S11e), $\text{Co-(NiFe)N@NiS}_x\text{@NF}$ exhibited 387.5 cm^2 of ECSA, which is over four times larger than that for the non-interlayered counterpart and control $\text{NiS}_x\text{@NF}$. This points towards a notable increase of electroactive sites when NiS_x is present as an interlayer or as a growth substrate. Fig. S11f presents the ECSA normalized polarization curves under the same alkaline SSW electrolyte, whereby a similar trend is noted between the interlayered and non-interlayered electrocatalysts. Briefly, a lower ECSA-specific onset overpotential is

observed for $\text{Co-(NiFe)N@NiS}_x\text{@NF}$, however lower overpotentials are exhibited on the non-interlayered counterpart. Control $\text{NiS}_x\text{@NF}$ exhibited a similar performance to that of the non-interlayered Co-(NiFe)N@NF . Considering that no buried catalytic layer is present for the former anode, the diffusion-limited phenomenon can be omitted to a certain degree. All in all, higher BET and ECSA present on $\text{Co-(NiFe)N@NiS}_x\text{@NF}$, along with higher conductivity, and favorable surface oxidation states of Co sites results in enhanced electrochemical activities.

Furthermore, Nyquist plots obtained from EIS at 1.55 V (vs. RHE) DC voltage and an amplitude AC voltage of 10 mV in neutral pH SSW electrolyte (Fig. 5e) shows a higher conductivity (lower charge transfer resistance (R_{ct})) for the NiS_x interlayered sample. Since all samples were electrochemically tested in the same three-electrode cell with the same configuration, the uncompensated solution resistance (R_u) is almost the same and was used for iR correction of polarization curves. To evaluate catalyst stability, 24-hour chronoamperometry (CA) tests were performed in alkaline SSW (Fig. 5f) and neutral pH SSW (Fig. 5g) electrolytes. Fixing the applied potential of Co-(NiFe)N@NF and $\text{Co-(NiFe)N@NiS}_x\text{@NF}$ at 1.65 and 1.58 V (vs. RHE), respectively, which correspond to an initial current density of 100 mA cm^{-2} , the current retention attained was 89.4% and 97.5% of the initial 100 mA cm^{-2} . In order to probe the FE of OER and consequently test the effectiveness of CER suppression, similar analyses were undertaken in neutral pH SSW at an initial applied potential of 1.75 V (vs. RHE) such that the applied potential is above the CER thermodynamic limit at neutral pH (η_{CER} 1.701 V (vs. RHE)). To this end, the applied 1.75 V (vs. RHE) under neutral pH SSW corresponds to initial current densities of 94 and 168 mA cm^{-2} for Co-(NiFe)N@NF and $\text{Co-(NiFe)N@NiS}_x\text{@NF}$, respectively, whereby 56.9% and 88.5% current retention was ensured after 24 h of operation. Moreover, commercial 20 wt% $\text{IrO}_2/\text{C@NF}$ electrodes were prepared and tested for activity and stability comparison in alkaline DIE and alkaline SSW electrolytes. A notable drop in activity is reflected in the polarization curves presented in Fig. S12a, whereby 425 mV was required to obtain current density of 100 mA cm^{-2} in alkaline SSW electrolyte, which is 35 mV higher than that was required in alkaline non-saline water electrolyte. Contrarily, a substantial overpotential of 410 mV and 615 mV were required to attain a mere 10 mA cm^{-2} of current density in neutral pH non-saline water and neutral pH SSW electrolytes, respectively, as shown in Fig. S12b. 24-hours CA tests for $\text{IrO}_2/\text{C@NF}$ presented in Fig. S12c show good stability at 100 mA cm^{-2} of current density in alkaline non-saline water electrolyte, but deteriorating stabilities in non-saline water and SSW electrolytes at neutral pH conditions. Therefore, it can be noted that the developed $\text{Co-(NiFe)N@NiS}_x\text{@NF}$ attains higher activity and stability in both alkaline, and particularly neutral pH environments for non-saline water and SSW. In an effort to investigate the role of interlayering NiS_x has on electrochemical performance, the same tests under alkaline and neutral pH non-saline and SSW electrolytes were conducted and the results are shown in Figs. S12a and S12b. To reach 100 mA cm^{-2} of current density in alkaline environments, 440 and 480 mV of overpotential were required in non-saline water and SSW electrolytes, respectively. The 40 mV potential increase in the presence of SSW is very close to the 35 mV required for noble metal IrO_2/C in the presence of SSW noted earlier. However, in neutral pH electrolyte, an overpotential increase from 290 to 355 mV was required to sustain 10 mA cm^{-2} of current density, which is an order of magnitude lower than that when using IrO_2/C under the same testing conditions. This suggests that the activity enhancement of $\text{Co-(NiFe)N@NiS}_x\text{@NF}$ is in part due to the NiS_x interlayer, albeit activity of $\text{Co-(NiFe)N@NiS}_x\text{@NF}$ is substantially higher than $\text{NiS}_x\text{@NF}$ in both alkaline and neutral pH electrolytes. Although stable performance is shown for $\text{NiS}_x\text{@NF}$ at 100 mA cm^{-2} under neutral pH non-saline water conditions during a standard 24-hours CA study (Fig. S12d), a near 25% drop from the initial current density was noted for the same catalyst in neutral pH SSW electrolyte. The observed drop in current density for the latter scenario

seemed to occur rapidly from the 13-hour mark suggesting a possible local corrosion of the underlying NF support during operation, which can lead to detachment or leaching of surface metal sulfide. Again, this showcases that in large part NiS_x/NF is not stable in chloride-containing neutral pH electrolytes in the absence of an electroactive surface layer (i.e., $\text{Co}-(\text{NiFe})\text{N}$).

Control electrocatalysts of $(\text{NiFe})\text{N} @ \text{NiS}_x/\text{NF}$ (Fig. S13a), $\text{Co}-(\text{Fe})\text{N} @ \text{NiS}_x/\text{NF}$ (Fig. S13b), and $\text{Co}-(\text{Ni})\text{N} @ \text{NiS}_x/\text{NF}$ (Fig. S13c) were prepared and electrochemically tested in both alkaline and neutral pH SSW, as shown in Fig. S13d. This set of experiments was in part undertaken to determine the role of individual elements Co, Ni, and Fe, respectively, on the performance of the optimum catalyst $\text{Co}-(\text{NiFe})\text{N} @ \text{NiS}_x/\text{NF}$. Alkaline SSW overpotentials of 440, 480, and 520 mV were required for $(\text{NiFe})\text{N} @ \text{NiS}_x/\text{NF}$, $\text{Co}-(\text{Fe})\text{N} @ \text{NiS}_x/\text{NF}$, and $\text{Co}-(\text{Ni})\text{N} @ \text{NiS}_x/\text{NF}$, respectively, to obtain current density of 100 mA cm^{-2} – relative to 350 mV required for $\text{Co}-(\text{NiFe})\text{N} @ \text{NiS}_x/\text{NF}$ to achieve the same current density. Similarly under neutral pH SSW, overpotentials of 680, 645, and 590 mV were required to sustain 100 mA cm^{-2} for $(\text{NiFe})\text{N} @ \text{NiS}_x/\text{NF}$, $\text{Co}-(\text{Fe})\text{N} @ \text{NiS}_x/\text{NF}$, and $\text{Co}-(\text{Ni})\text{N} @ \text{NiS}_x/\text{NF}$, respectively – relative to 425 mV needed for $\text{Co}-(\text{NiFe})\text{N} @ \text{NiS}_x/\text{NF}$. These polarization results indicate that doping of Fe plays a fundamental role during alkaline pH operation and Co presence is pivotal towards neutral pH operation. Moreover, taking the ratio of overpotentials under alkaline and neutral pH SSW for each electrocatalyst, it is found that the smallest change in activity of 11.9% for $\text{Co}-(\text{Ni})\text{N} @ \text{NiS}_x/\text{NF}$, followed by 17.6% change for $\text{Co}-(\text{NiFe})\text{N} @ \text{NiS}_x/\text{NF}$, and 35.3% for $(\text{NiFe})\text{N} @ \text{NiS}_x/\text{NF}$. Therefore, in choosing the optimum catalyst in terms of OER activity across neutral and alkaline pH operation, $\text{Co}-(\text{NiFe})\text{N} @ \text{NiS}_x/\text{NF}$ is the obvious choice. Further, relating back to XRD analysis in Fig. S7 of the control samples, the higher electrochemical performance of $\text{Co}-(\text{Ni})\text{N} @ \text{NiS}_x/\text{NF}$ relative to $\text{Co}-(\text{Fe})\text{N} @ \text{NiS}_x/\text{NF}$ in neutral pH electrolyte suggests that the Ni_3N phase plays an important role during neutral pH water oxidation. Also, the substantial drop in performance for $(\text{NiFe})\text{N} @ \text{NiS}_x/\text{NF}$ under neutral pH SSW conditions highlights the importance of CoN , Co_3O_4 , and $\alpha\text{-CoOOH}$ for H_2O dissociation and oxidation, which agrees with the findings by Niu et al. on similar nitride/oxide surfaces. Under alkaline conditions, XRD spectra of $\text{Co}-(\text{NiFe})\text{N} @ \text{NiS}_x/\text{NF}$ shows minor Ni-LDH presence, although notable peaks are found for $(\text{NiFe})\text{N} @ \text{NiS}_x/\text{NF}$, which exhibited highest bimetallic control group activity in alkaline SSW. Significant presence of $\alpha\text{-CoOOH}$ and Co_3O_4 therefore contribute to the majority of activity in alkaline SSW electrolyte, whilst NiFe plays a dual role of enhancing conductivity through Ni_3N and electronic regulation towards Co, as shown from XAS and XPS analyses.

Online GC measurements of O_2 were undertaken at known time intervals and corresponding FE were calculated and presented in Fig. 5 h. A summary of the average FE values are displayed in Fig. 5i whereby at first glance, it can be seen that irrespective of the electrolyte, the NiS_x interlayered samples attained higher FE towards OER. Control CA stability tests were performed in alkaline and neutral pH buffered non-saline electrolytes, shown in Fig. S14 and congruent FE are shown in Fig. 5i. Of key importance is to note the effect of salinity on FE for a given anodic electrocatalyst tested under the same electrochemical conditions. For example, $\text{Co}-(\text{NiFe})\text{N} @ \text{NF}$ exhibited a 91.5% FE in alkaline non-saline electrolyte at an initial current density of 100 mA cm^{-2} which drops by 7.3% during operation in SSW electrolyte. This suggests that in SSW electrolyte, the $\text{Co}-(\text{NiFe})\text{N}$ surface consumes 7.3% of the passed charge towards oxidation reactions other than OER. This is under an applied potential of 1.64 V (vs. RHE), which is below the η_{CER} at alkaline pH and thus, it can't be attributed to CER. Such drop in FE could be attributed to the oxidation of other SSW constituents such as bromide, which was found in SSW at a concentration of 65 mg L^{-1} , and is known to have a thermodynamic potential limit for oxidation to brominated species at lower potentials than the applied potential herein. Analogously, for the $\text{Co}-(\text{NiFe})\text{N} @ \text{NiS}_x$ surface under the same

conditions attains an initially higher FE of 96.2% in alkaline non-saline electrolyte, which drops by 2% in SSW under the same conditions. Furthermore, under the kinetically challenging neutral pH regime, $\text{Co}-(\text{NiFe})\text{N} @ \text{NF}$ ensures a FE of 88.1% in non-saline phosphate electrolyte, and a substantial decrease of FE towards OER by 12.3% when SSW is used. This significant FE drop in neutral pH buffered NaCl and SSW electrolytes can be attributed to CER and instability of the catalyst with operation time in the absence of the interlayer. Contrarily, and to showcase the enhancement in OER selectivity for the interlayered electrocatalyst, $\text{Co}-(\text{NiFe})\text{N} @ \text{NiS}_x$ maintains a FE of 92.1% in neutral pH non-saline electrolyte and it dropped by 3.5% in neutral pH buffered SSW. The attained results clearly show that although 100% FE towards OER is not achieved, nearly 4 times enhanced CER suppression is ensured on the NiS_x interlayered surface. Furthermore, during the 24-hours CA stability tests on NiS_x/NF with an initial current density of 100 mA cm^{-2} , online GC measurements towards OER FE has been undertaken with the goal of eliminating the influence of the substrate, as shown in Fig. S12e. In so doing, average FE values have been recorded at 94.22%, 92.67%, 91.89%, and 88.37% for alkaline non-saline, alkaline SSW, neutral pH non-saline, and neutral pH SSW electrolytes, respectively. Contrasting this with FE results of $\text{Co}-(\text{NiFe})\text{N} @ \text{NiS}_x/\text{NF}$, it is noted that under alkaline environments, FE of NiS_x/NF is $\sim 2\%$ lower than that of $\text{Co}-(\text{NiFe})\text{N} @ \text{NiS}_x/\text{NF}$ under the same current density. This indicates a dual effect of the surface role of electroactive $\text{Co}-(\text{NiFe})\text{N}$ towards OER selectivity under alkaline pH regimes, as well as a non-equivalency towards FE when NiS_x is used as an interlayer and when utilized as a surface catalytic layer. However, under neutral pH conditions FE of NiS_x/NF is approximately the same as that of $\text{Co}-(\text{NiFe})\text{N} @ \text{NiS}_x/\text{NF}$ suggesting the pivotal role NiS_x interlayer has under neutral pH regimes. Moreover, it is important to note that FE measurements in non-saline electrolyte is not around the 100% mark, which could be attributed to several factors that are usually overlooked. Since the overwhelming majority of electrocatalyst development work is performed under standard 3-electrode cells, micro- and nano-bubble presence from evolved gasses around catalytic active sites along with iR drops from non-zero-gap design of electrolyzer cell can result in non-ideal FE [58]. To examine prolonged stability of $\text{Co}-(\text{NiFe})\text{N} @ \text{NiS}_x/\text{NF}$ under elevated current density (200 mA cm^{-2}) in both alkaline and neutral pH SSW electrolytes, 168-hour CA tests were conducted (Fig. 5j). High stability is clearly noted for both systems, whereby approximately 4.1% and 15.7% current reduction is exhibited in alkaline and neutral pH SSW, respectively.

4. Conclusion

Through a facile two-step hydrothermal/nitridations synthesis procedure, a homogeneously surface heterointerfaced $\text{Co}-(\text{NiFe})$ oxide/nitride anodic electrocatalyst with NiS_x interlayers was fabricated to ameliorate three main predicaments of neutral pH seawater electrolysis – namely high activity, stability, and selectivity towards OER. The best performing $\text{Co}-(\text{NiFe})\text{N} @ \text{NiS}_x/\text{NF}$ catalyst attained high activities in both alkaline (1 M KOH + 35 g/L SSW) and neutral pH synthetic seawater (1 M PB + 35 g/L SSW), whereby 350 and 425 mV of overpotential were required to reach 100 mA cm^{-2} of current density, respectively. Typically, decrease in the local pH around the anode under neutral pH conditions combined with chloride corrosive effects leads to dissolution of catalytic metallic component, which lowers stability. Postmortem OER XPS analysis revealed that interlaying the anode with NiS_x eliminates dissolution and effectively enhances stability. Further, high OER selectivity was assured on $\text{Co}-(\text{NiFe})\text{N} @ \text{NiS}_x/\text{NF}$, whereby $\sim 90\%$ FE were attained under 1.75 V (vs. RHE) at neutral pH SSW environments based on long-duration chronoamperometry studies. The role of the NiS_x interlayer was examined through performing electrochemical polarization, stability, and FE analyses on $\text{Co}-(\text{NiFe})\text{N} @ \text{NF}$ in the absence of NiS_x . Our results indicate that not only does NiS_x directly ensure higher selectivity for OER, but also enhances activity through

improving hydrophilicity, conductivity, and modulating surface electronics towards more favorable water dissociation. Moreover, increases in BET- and electrochemical surface area was witnessed for the NiS_x interlayered sample which provides more active sites per unit area for reaction irrespective of reaction media. Furthermore, pre- and post-OER characterization under neutral pH SSW was undertaken through XPS and XRD analysis. Favorably higher Co²⁺/Co³⁺ ratios were found to occur for the interlayered sample suggesting that NiS_x plays a role in allowing Ni and Fe to act as Co valence state regulating species. Control electrocatalysts of component transition metal-based surface were synthesized, electrochemically tested, and characterized to provide insight on active sites, which were found to be pH dependent. Fe-doping was found to be pivotal towards alkaline operation, while Co-doping was found to be crucial towards high activity under neutral pH SSW environments. Phase transformation from crystalline NiS_x to quasi-amorphous polyanionic sulfite/sulfate species was found to activate during anodic operation in Cl[−] containing electrolytes. Overall, this work provides insight into the rational design and synthesis of robust electrocatalysts towards neutral pH impure-water oxidation.

CRediT authorship contribution statement

Ahmed Badreldin: Investigation, Data curation, Conceptualization, Formal analysis, Validation, Writing – original draft. **Jehad Abed:** Formal analysis, Writing – review & editing. **Noor Hassan:** Investigation, Validation. **Abdellatif El-Ghenymy:** Formal analysis, Validation. **Wafa Suwaileh:** Investigation. **Zafar Khan Ghouri:** Investigation. **Yiming Wubulikasimu:** Data curation, Formal analysis. **Karim Youssef:** Investigation. **Dharmesh Kumar:** Supervision, Writing – review & editing. **Khaled Elsaid:** Formal analysis, Software, Validation. **Edward H. Sargent:** Supervision, Writing – review & editing. **Ahmed Abdel-Wahab:** Conceptualization, Supervision, Funding acquisition, Writing – review & editing.

Declaration of Competing Interest

The authors declare that they have no known competing financial interests or personal relationships that could have appeared to influence the work reported in this paper.

Data Availability

Data will be made available on request.

Acknowledgment

This study was made possible by a grant from the Qatar National Research Fund under its National Priorities Research Program award number NPRP12S-0131–190024 and by Shell Global Solutions International B.V. The paper's contents are solely the responsibility of the authors and do not necessarily represent the official views of the Qatar National Research Fund. This research used resources of the Advanced Photon Source, an Office of Science User Facility operated for the U.S. Department of Energy (DOE) Office of Science by Argonne National Laboratory (ANL) and was supported by the U.S. DOE under Contract No. DE-AC02-06CH11357, and the Canadian Light Source and its funding partners. The authors thank Dr. Tianpin Wu and Dr. George Sterbinsky from 9BM beamline (ANL) and Dr. Debora Motta Meira and Dr. Zou Finrock from 20BM beamline (ANL) for assistance in collecting the XAS data and at the advanced photo source (APS). Open Access funding provided by the Qatar National Library.

Appendix A. Supporting information

Supplementary data associated with this article can be found in the online version at [doi:10.1016/j.apcatb.2023.122599](https://doi.org/10.1016/j.apcatb.2023.122599).

References

- [1] J.D. Hunt, A. Nascimento, N. Nascimento, L.W. Vieira, O.J. Romero, Possible pathways for oil and gas companies in a sustainable future: from the perspective of a hydrogen economy, *Renew. Sustain. Energy Rev.* 160 (2022), <https://doi.org/10.1016/j.rser.2022.112291>.
- [2] Z. Chen, W. Wei, B.J. Ni, Cost-effective catalysts for renewable hydrogen production via electrochemical water splitting: recent advances, *Curr. Opin. Green. Sustain. Chem.* 27 (2021), <https://doi.org/10.1016/j.cogsc.2020.100398>.
- [3] W. Tong, M. Forster, F. Dionigi, S. Dresp, R. Sadeghi Erami, P. Strasser, P. Farràs, Electrolysis of low-grade and saline surface water, *Nat. Energy* 5 (2020) 367–377, <https://doi.org/10.1038/s41560-020-0550-8>.
- [4] P. Farràs, P. Strasser, A.J. Cowan, Water electrolysis: direct from the sea or not to be? *Joule* 5 (2021) 1921–1923, <https://doi.org/10.1016/j.joule.2021.07.014>.
- [5] J.N. Hausmann, R. Schlögl, P.W. Menezes, M. Driess, Is direct seawater splitting economically meaningful? *Energy Environ. Sci.* 14 (2021) 3679–3685, <https://doi.org/10.1039/D0EE03659E>.
- [6] G.A. Lindquist, Q. Xu, S.Z. Oener, S.W. Boettcher, Membrane electrolyzers for impure-water splitting, *Joule* 4 (2020) 2549–2561, <https://doi.org/10.1016/j.joule.2020.09.020>.
- [7] Y. Xu, C. Wang, Y. Huang, J. Fu, Recent advances in electrocatalysts for neutral and large-current-density water electrolysis, *Nano Energy* 80 (2021), 105545, <https://doi.org/10.1016/j.nanoen.2020.105545>.
- [8] Y. Dong, S. Komarneni, Strategies to develop earth-abundant heterogeneous oxygen evolution reaction catalysts for pH-neutral or pH-near-neutral electrolytes, *Small Methods* 5 (2021), 2000719, <https://doi.org/10.1002/smt.202000719>.
- [9] S. Khatun, H. Hirani, P. Roy, Seawater electrocatalysis: activity and selectivity, *J. Mater. Chem. A* 9 (2021) 74–86, <https://doi.org/10.1039/D0TA08709B>.
- [10] J.C. Fornaciari, L.C. Weng, S.M. Alia, C. Zhan, T.A. Pham, A.T. Bell, A.Z. Weber, Mechanistic understanding of pH effects on the oxygen evolution reaction, *Electrochim. Acta* 405 (2022), 139810, <https://doi.org/10.1016/j.electacta.2021.139810>.
- [11] A. Badreldin, A.E. Abusrafa, A. Abdel-Wahab, Oxygen-deficient cobalt-based oxides for electrocatalytic water splitting, *ChemSusChem* 14 (2021) 10–32, <https://doi.org/10.1002/cssc.202002002>.
- [12] A. Badreldin, A.E. Abusrafa, A. Abdel-Wahab, Oxygen-deficient perovskites for oxygen evolution reaction in alkaline media: a review, *Emergent Mater.* 3 (2020) 567–590, <https://doi.org/10.1007/s42247-020-00123-z>.
- [13] A.K. Tareen, G.S. Priyanga, K. Khan, E. Pervaiz, T. Thomas, M. Yang, Nickel-based transition metal nitride electrocatalysts for the oxygen evolution reaction, *ChemSusChem* 12 (2019) 3941–3954, <https://doi.org/10.1002/cssc.201900553>.
- [14] Y. Liu, Y. Li, H. Kang, T. Jin, L. Jiao, Design, synthesis, and energy-related applications of metal sulfides, *Mater. Horiz.* 3 (2016) 402–421, <https://doi.org/10.1039/C6MH00075D>.
- [15] Z.K. Ghouri, K. Elsaid, M.M. Nasef, S. Ahmed, A. Badreldin, A. Abdel-Wahab, Cooperative electrocatalytic effect of Pd and Ce alloys nanoparticles in PdCe@CNWs electrode for oxygen evolution reaction (OER), *Mol. Catal.* 522 (2022), 112255, <https://doi.org/10.1016/j.mcat.2022.112255>.
- [16] Z.K. Ghouri, A. Badreldin, K. Elsaid, D. Kumar, K. Youssef, A. Abdel-Wahab, Theoretical and experimental investigations of Co-Cu bimetallic alloys-incorporated carbon nanowires as an efficient bi-functional electrocatalyst for water splitting, *J. Ind. Eng. Chem.* 96 (2021) 243–253, <https://doi.org/10.1016/j.jiec.2021.01.027>.
- [17] L. Peng, S.S.A. Shah, Z. Wei, Recent developments in metal phosphide and sulfide electrocatalysts for oxygen evolution reaction, *Chin. J. Catal.* 39 (2018) 1575–1593, [https://doi.org/10.1016/S1872-2067\(18\)63130-4](https://doi.org/10.1016/S1872-2067(18)63130-4).
- [18] W. Zheng, L.Y.S. Lee, K.Y. Wong, Improving the performance stability of direct seawater electrolysis: from catalyst design to electrode engineering, *Nanoscale* 13 (2021) 15177–15187, <https://doi.org/10.1039/D1NR03294A>.
- [19] A.A. Bhardwaj, J.G. Vos, M.E. Beatty, A.F. Baxter, M.T. Koper, N.Y. Yip, D. V. Esposito, Ultrathin silicon oxide overlayers enable selective oxygen evolution from acidic and unbuffered pH-neutral seawater, *ACS Catal.* 11 (2021) 1316–1330, <https://doi.org/10.1021/acscatal.0c04343>.
- [20] L. Yu, Q. Zhu, S. Song, B. McElhenny, D. Wang, C. Wu, Z. Ren, Non-noble metal-nitride based electrocatalysts for high-performance alkaline seawater electrolysis, *Nat. Commun.* 10 (2019) 1–10, <https://doi.org/10.1038/s41467-019-13092-7>.
- [21] C. Wang, M. Zhu, Z. Cao, P. Zhu, Y. Cao, X. Xu, Z. Yin, Heterogeneous bimetallic sulfides based seawater electrolysis towards stable industrial-level large current density, *Appl. Catal. B: Environ.* 291 (2021), 120071, <https://doi.org/10.1016/j.apcatb.2021.120071>.
- [22] Y. Kuang, M.J. Kenney, Y. Meng, W.H. Hung, Y. Liu, J.E. Huang, H. Dai, Solar-driven, highly sustained splitting of seawater into hydrogen and oxygen fuels, *Proc. Natl. Acad. Sci.* 116 (2019) 6624–6629, <https://doi.org/10.1073/pnas.1900556116>.
- [23] J. Li, Y. Liu, H. Chen, Z. Zhang, X. Zou, Design of a multilayered oxygen-evolution electrode with high catalytic activity and corrosion resistance for saline water splitting, *Adv. Funct. Mater.* 31 (2021), 2101820, <https://doi.org/10.1002/adfm.202101820>.
- [24] F. Dionigi, T. Reier, Z. Pawolek, M. Glicke, P. Strasser, Design criteria, operating conditions, and nickel-iron hydroxide catalyst materials for selective seawater electrolysis, *ChemSusChem* 9 (2016) 962–972, <https://doi.org/10.1002/cssc.201501581>.
- [25] A. Badreldin, A. Nabeeh, Z.K. Ghouri, J. Abed, N. Wang, Y. Wubulikasimu, A. Abdel-Wahab, Early transition-metal-based binary oxide/nitride for efficient electrocatalytic hydrogen evolution from saline water in different pH

- environments, *ACS Appl. Mater. Interfaces* 13 (2021) 53702–53716, <https://doi.org/10.1021/acsami.1c13002>.
- [26] S. Niu, Y. Fang, J. Zhou, J. Cai, Y. Zang, Y. Wu, Y. Qian, Manipulating the water dissociation kinetics of Ni₃N nanosheets via in situ interfacial engineering, *J. Mater. Chem. A* 7 (2019) 10924–10929, <https://doi.org/10.1039/C9TA03249E>.
- [27] A. Badreldin, K. Youssef, A. El Ghenymy, Y. Wubulikasimu, Z.K. Ghouri, K. Elsaid, A. Abdel-Wahab, Solution combustion synthesis of novel S, B-codoped CoFe oxyhydroxides for the oxygen evolution reaction in saline water, *ACS Omega* 7 (2022) 5521–5536, <https://doi.org/10.1021/acsomega.1c06968>.
- [28] A. Badreldin, A. Nabeeh, E. Youssef, N. Mubarak, H. ElSayed, R. Mohsen, A. Abdel-Wahab, Adapting early transition metal and nonmetallic dopants on CoFe oxyhydroxides for enhanced alkaline and neutral pH saline water oxidation, *ACS Applied Energy Mater.* 4 (2021) 6942–6956, <https://doi.org/10.1021/acsaem.1c01036>.
- [29] S. Hosseini, A. Abbasi, L.O. Uginet, N. Haustraete, S. Praserttham, T. Yonezawa, S. Kheawhom, The influence of dimethyl sulfoxide as electrolyte additive on anodic dissolution of alkaline zinc-air flow battery, *Sci. Rep.* 9 (2019) 1–12, <https://doi.org/10.1038/s41598-019-51412-5>.
- [30] G. Zhang, J. Li, G. Zhang, L. Zhao, Room-temperature synthesis of Ni nanoparticles as the absorbent used for sewage treatment, *Adv. Mater. Sci. Eng.* (2015) (2015), <https://doi.org/10.1155/2015/973648>.
- [31] R. Sanchis-Gual, A. Seijas-Da Silva, M. Coronado-Puchau, T.F. Otero, G. Abellán, E. Coronado, Improving the onset potential and Tafel slope determination of earth-abundant water oxidation electrocatalysts, *Electrochim. Acta* 388 (2021), 138613, <https://doi.org/10.1016/j.electacta.2021.138613>.
- [32] J. Jang, T.H. Kim, J.H. Ryu, Surface nitridation of Li₄Ti₅O₁₂ by thermal decomposition of urea to improve quick charging capability of lithium ion batteries, *Scientific Reports*, z 11 (2021) 1–7, <https://doi.org/10.1038/s41598-021-92550->.
- [33] S. Jung, C.C. McCrory, I.M. Ferrer, J.C. Peters, T.F. Jaramillo, Benchmarking nanoparticulate metal oxide electrocatalysts for the alkaline water oxidation reaction, *J. Mater. Chem. A* 4 (2016) 3068–3076, <https://doi.org/10.1039/C5TA07586F>.
- [34] J. Huang, Statistical treatment of activity and durability of electrocatalysts with distributed binding energies, *J. Electrochem. Soc.* 168 (2021), 066507, <https://doi.org/10.1149/1945-7111/ac0362>.
- [35] C. Huang, B. Zhang, Y. Wu, Q. Ruan, L. Liu, J. Su, P.K. Chu, Experimental and theoretical investigation of reconstruction and active phases on honeycombed Ni₃N-Co₃N/C in water splitting, *Appl. Catal. B: Environ.* 297 (2021), 120461, <https://doi.org/10.1016/j.apcatb.2021.120461>.
- [36] G. Jiang, H. Han, W. Zhuang, X. Xu, S. Kaskel, F. Xu, H. Wang, Three-dimensional ordered mesoporous cobalt nitride for fast-kinetics and stable-cycling lithium storage, *J. Mater. Chem. A* 7 (2019) 17561–17569, <https://doi.org/10.1039/C9TA03391B>.
- [37] X. Wang, Y. Yang, R. Wang, L. Li, X. Zhao, W. Zhang, Porous Ni₃S₂-Co₉S₈ carbon aerogels derived from Carrageenan/NiCo-MOF hydrogels as an efficient electrocatalyst for oxygen evolution in rechargeable Zn–Air batteries, *Langmuir* 38 (2022) 7280–7289, <https://doi.org/10.1021/acs.langmuir.2c00805>.
- [38] C.T. Dinh, A. Jain, F. de Arquer, P. De Luna, J. Li, N. Wang, E.H. Sargent, Multi-site electrocatalysts for hydrogen evolution in neutral media by destabilization of water molecules, *Nat. Energy* 4 (2019) 107–114, <https://doi.org/10.1038/s41560-018-0296-8>.
- [39] Z. Li, X. Li, L. Xiang, X. Xie, X. Li, D.R. Xiao, S. Liu, Three-dimensional hierarchical nickel–cobalt–sulfide nanostructures for high performance electrochemical energy storage electrodes, *J. Mater. Chem. A* 4 (2016) 18335–18341, <https://doi.org/10.1039/C6TA08517B>.
- [40] Y. Yu, Y. Tan, B. Yang, L. Yuan, X. Shen, X. Hu, Electrochemical transformation method for the preparation of novel 3D hybrid porous CoOOH/Co (OH)₂ composites with excellent pseudocapacitive performance, *J. Power Sources* 443 (2019), 227278, <https://doi.org/10.1016/j.jpowsour.2019.227278>.
- [41] A. Diallo, A.C. Beye, T.B. Doyle, E. Park, M. Maaza, Green synthesis of Co₃O₄ nanoparticles via *Aspalathus linearis*: physical properties, *Green. Chem. Lett. Rev.* 8 (2015) 30–36, <https://doi.org/10.1080/17518253.2015.1082646>.
- [42] B. Zhang, L. Wang, Z. Cao, S.M. Kozlov, F.P. García de Arquer, C.T. Dinh, E. H. Sargent, High-valence metals improve oxygen evolution reaction performance by modulating 3d metal oxidation cycle energetics, *Nat. Catal.* 3 (2020) 985–992, <https://doi.org/10.1038/s41929-020-00525-6>.
- [43] Y. Zhang, B. Ouyang, G. Long, H. Tan, Z. Wang, Z. Zhang, H.J. Fan, Enhancing bifunctionality of CoN nanowires by Mn doping for long-lasting Zn-air batteries, *Sci. China Chem.* 63 (2020) 890–896, <https://doi.org/10.1007/s11426-020-9739-2>.
- [44] T. Wang, M. Wang, H. Yang, M. Xu, C. Zuo, K. Feng, Y. Li, Weakening hydrogen adsorption on nickel via interstitial nitrogen doping promotes bifunctional hydrogen electrocatalysis in alkaline solution, *Energy Environ. Sci.* 12 (2019) 3522–3529, <https://doi.org/10.1039/C9EE01743G>.
- [45] B. Chang, L. Deng, S. Wang, D. Shi, Z. Ai, H. Jiang, X. Hao, A vanadium–nickel oxynitride layer for enhanced electrocatalytic nitrogen fixation in neutral media, *J. Mater. Chem. A* 8 (2020) 91–96, <https://doi.org/10.1039/C9TA11378A>.
- [46] Y. Li, Y. He, J. Qiu, J. Zhao, Q. Ye, Y. Zhu, J. Mao, Enhancement of pitting corrosion resistance of austenitic stainless steel through deposition of amorphous/nanocrystalline oxy-nitrided phases by active screen plasma treatment, *Mater. Res.* 21 (2018), <https://doi.org/10.1590/1980-5373-MR-2017-0697>.
- [47] M. Fantauzzi, B. Elsener, D. Atzei, A. Rigoldi, A. Rossi, Exploiting XPS for the identification of sulfides and polysulfides, *RSC Adv.* 5 (2015) 75953–75963, <https://doi.org/10.1039/C5RA14915K>.
- [48] J.C. Hsu, Y.H. Lin, P.W. Wang, X-ray photoelectron spectroscopy analysis of nitrogen-doped TiO₂ films prepared by reactive-ion-beam sputtering with various NH₃/O₂ gas mixture ratios, *Coatings* 10 (47) (2020), <https://doi.org/10.3390/coatings10010047>.
- [49] V. Beschkov, E. Razkazova-Velkova, M. Martinov, S. Stefanov, Electricity production from marine water by sulfide-driven fuel cell, *Appl. Sci.* 8 (2018) 1926, <https://doi.org/10.3390/app8101926>.
- [50] T. Ma, W. Xu, B. Li, X. Chen, J. Zhao, S. Wan, L. Chen, The critical role of additive sulfate for stable alkaline seawater oxidation on nickel-based electrodes, *Angew. Chem.* 133 (2021) 22922–22926, <https://doi.org/10.1002/ange.202110355>.
- [51] K. Ayers, N. Danilovic, R. Ouimet, M. Carmo, B. Pivovar, M. Bornstein, Perspectives on low-temperature electrolysis and potential for renewable hydrogen at scale, *Annu. Rev. Chem. Biomol. Eng.* 10 (2019), <https://doi.org/10.1146/annurev-chembioeng-060718-030241>.
- [52] A.R. Jadhav, A. Kumar, J. Lee, T. Yang, S. Na, J. Lee, H. Lee, Stable complete seawater electrolysis by using interfacial chloride ion blocking layer on catalyst surface, *J. Mater. Chem. A* 8 (2020) 24501–24514, <https://doi.org/10.1039/D0TA08543J>.
- [53] Y. Wu, Z. Tian, S. Yuan, Z. Qi, Y. Feng, Y. Wang, Solar-driven self-powered alkaline seawater electrolysis via multifunctional earth-abundant heterostructures, *Chem. Eng. J.* 411 (2021), 128538, <https://doi.org/10.1016/j.cej.2021.128538>.
- [54] F. Cheng, X. Feng, X. Chen, W. Lin, J. Rong, Synergistic action of Co-Fe layered double hydroxide electrocatalyst and multiple ions of sea salt for efficient seawater oxidation at near-neutral pH, *Electrochim. Acta* 251 (2017) 336–343, <https://doi.org/10.1016/j.electacta.2017.08.098>.
- [55] R. Wu, B. Xiao, Q. Gao, Y.R. Zheng, X.S. Zheng, J.F. Zhu, A janus nickel cobalt phosphide catalyst for high-efficiency neutral-pH water splitting, *Angew. Chem.* 130 (2018) 15671–15675, <https://doi.org/10.1002/ange.201808929>.
- [56] L. Yan, B. Zhang, J. Zhu, Y. Li, P. Tsiakaras, Electronic modulation of cobalt phosphide nanosheet arrays via copper doping for highly efficient neutral-pH overall water splitting, *Appl. Catal. B: Environ.* 265 (2020), 118555, <https://doi.org/10.1016/j.apcatb.2019.118555>.
- [57] Y. Tan, M. Luo, P. Liu, C. Cheng, J. Han, K. Watanabe, Three-dimensional nanoporous Co₉S₄P₄ pentlandite as a bifunctional electrocatalyst for overall neutral water splitting, *ACS Appl. Mater. Interfaces* 11 (2019) 3880–3888, <https://doi.org/10.1021/acsami.8b17961>.
- [58] T. Lazaridis, B.M. Stühmeier, H.A. Gasteiger, Capabilities and limitations of rotating disk electrodes versus membrane electrode assemblies in the investigation of electrocatalysts, *Nat. Catal.* 5 (2022) 363–373, <https://doi.org/10.1038/s41929-022-00776-5>.